



ATLAS NOTE

October 4, 2014



Test of a resistive micromega v 3.0 prototype with VMM1 readout using $\geq 0.8 \text{ GeV}/c^2$ cosmic muons

K. DiPetrillo^a, N. Felt^a, M. Franklin^a, P. Giromini^{a,b}, J. Gonski^a, J. Guimarães da Costa^a,
T. Lazovich^a, H. McKee^a, T. Morrison^a, H. Skottowe^a, B. Tong^a

^a*Harvard University, Cambridge, Massachusetts 02138, USA*

^b*Laboratori Nazionali di Frascati, Istituto Nazionale di Fisica Nucleare, Frascati, Italy*

Abstract

We present a detailed study of the VMM1 readout electronics using a resistive micromega v3.0 prototype and cosmic muons. This note is a revision of ATL-COM-UPGRADE-2014-017. A few minor bugs are fixed, we include the VMM1 performance using 50 ns peaktimes, and the μ TPC angular and position resolutions are investigated in detail.

1 Introduction

This is our fourth note on the performance of resistive micromega detectors and the VMM1 readout electronics. In the previous notes [1, 2, 3], we used signals produced by ^{55}Fe decays. We now extend our studies to minimum ionizing muons. The cosmic ray telescope is described in Section 2. Sections 3 and 4 describe the micromega prototype v 3.0 and the calibration of the VMM1-based readout system, respectively. The response of the detector to cosmic muons is presented in the next sections which are followed by a concise conclusion.

2 The cosmic-ray telescope

The Harvard cosmic ray telescope (HCRT), shown in Fig. 1, has been built in 2013 and commissioned during the Winter of 2014. It consists of two hodoscopes separated by 2.5 m and interleaved with a



Figure 1: The Harvard cosmic ray telescope (HCRT), described in Sec. 2.

concrete block 5 feet thick. Each hodoscope consists of 6 scintillator counters, 20 cm wide in the y direction (covering from $y=-60$ to $y=60$ cm) and 200 cm long (from $x=-100$ to $x=100$ cm) in the x direction. Each scintillator is read by two photomultipliers at its ends. We use the time difference between the two photomultipliers of each counter to reconstruct the x -coordinate of a muon¹. The trigger is defined by the coincidence of four signals corresponding to one counter on the bottom and one on the top layer. When a trigger arrives, the time distance between the signal of each counter and the

¹ We have measured $x = 6.28 \text{ (cm/ns)} \times \Delta t \text{ (ns)}$, where Δt is the time difference between the photomultiplier signals. The RMS x resolution is ≈ 15 cm. The y resolution is $20/\sqrt{12} = 6$ cm.

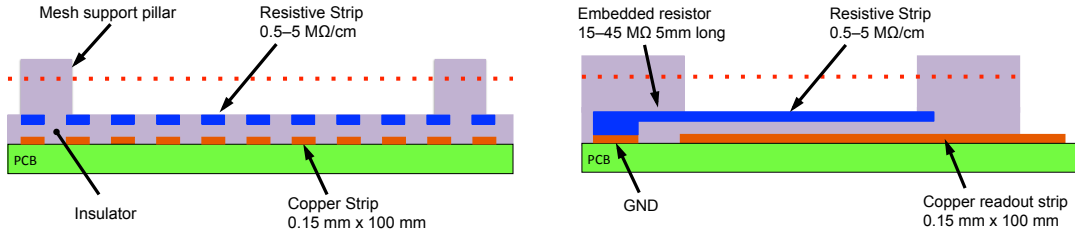


Figure 2: Sketch of micromega resistive and readout strips from the NSW TDR [5]. The width and pitch of the strips has changed (see text).

trigger is measured using a Lecroy 3377 multi-hit TDC, which has a 0.15 ns resolution, and subsequently acquired with a CAEN 111C camac crate controller.

The micromega detector is positioned on top of the concrete block with the readout strips parallel to the x axis. The micromega center is at $(x, y)=(0,0)$. Since its size is $10 \times 10 \text{ cm}^2$, we have added one scintillator counter of the same size, referred to as SP (small pad), on top of the micromega detector. The SP counter is also read out by two photomultipliers on opposite sides. We also require signals from the SP counter to generate a trigger. A trigger starts the readout of the CAMAC crate and of the VMM1 chip containing all micromega signals that arrived within a 900 ns window before the trigger. The arrival time of the micromega signal is compared to that of the SP counter which has a 1.2 ns resolution. Offline we remove those events in which there are more than two TDC hits on each of the three scintillator planes; this requirement removes approximately 10% of the events in which the muon is accompanied by a shower of other particles. In this configuration, the telescope accepts muons with energy $\geq 0.8 \text{ GeV}$ and with polar angle as large as $\pm 20^\circ$ with respect to the vertical direction. The average muon angle of incidence is 0° with a RMS deviation of $\pm 9^\circ$ in the $y - z$ plane perpendicular to the micromega strips. More details about the HCRT performance can be found in Ref. [4].

3 The v 3.0 resistive micromega prototype

The micromega prototype v 3.0, a sketch of which is shown in Fig. 2, is built according to the NSW TDR specifications [5]. The amplifying gap is $128 \mu\text{m}$ thick. The cathode is a woven stainless steel mesh with 400 lines/in and a wire thickness of $18 \mu\text{m}$. The mesh is kept at the $128 \mu\text{m}$ distance from the anode by a matrix of Pyralux pillars with $400 \mu\text{m}$ diameter and spaced by 2.5 mm in the x and y direction. The anode consists of resistive strips $15 \mu\text{m}$ thick deposited on a $50 \mu\text{m}$ thick Kapton foil. The resistive strips are 100 mm long in the x direction, $200 \mu\text{m}$ wide, and with a $400 \mu\text{m}$ pitch. The resistance of each strip is $5 \text{ M}\Omega/\text{cm}$. Each resistive strip is connected to ground with a $45 \text{ M}\Omega$ resistor. The resistive layer is built on top of the readout electrode. The readout electrode consists of $17 \mu\text{m}$ thick copper strips, $300 \mu\text{m}$ wide, with a $400 \mu\text{m}$ pitch and 10 cm long in the x direction. The 5 mm drift gap is built on top of the amplifying gap.

For these measurements, we use a $93\% \text{ Ar} + 7\% \text{ CO}_2$ gas mixture. Voltages are supplied by a CAEN DT5221 HV power supply. The mesh is at ground, the resistive anode, stabilized with a 100 nF capacitance, is set around 550 V . The drift voltage is set at -200 V and filtered with a RC circuit with a 100 ms time constant. As shown by Fig. 4, for drift voltages higher than 200 V , the mesh becomes less transparent.

In Refs. [1, 3], we did report that the breakdown voltage of amplifying gaps with grooves between anode strips was a function of the radiation exposure. The reason was tracked by Rui De Oliveira to pollution in the grooves that could not be burned/removed by just applying HV to the chamber filled with air. This prototype went through extreme cleaning [6], and its breakdown voltage (570 V) does not

depend on the radiation intensity.

As a benchmark, we have measured the ^{55}Fe charge collected by all x strips with an ORTEC 142C charge preamplifier followed by a ORTEC 472A shaping amplifier set to a $1\ \mu\text{s}$ shaping time. Figure 3 shows the ^{55}Fe spectrum at 540 V. Figure 4 shows the charge corresponding to the 6 KeV peak as a function of the anode voltage.

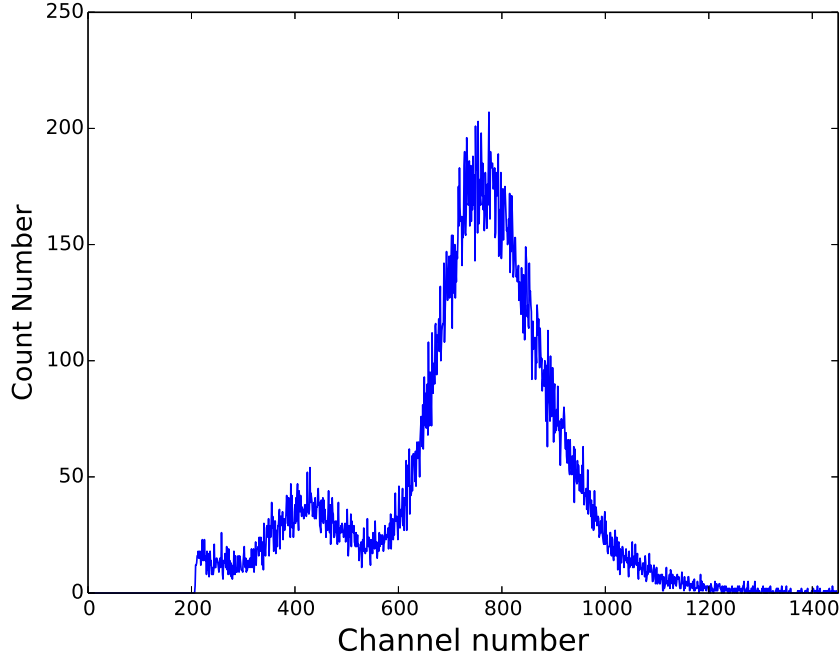


Figure 3: Charge distribution of the signals due to ^{55}Fe decays using an ORTEC 142C charge amplifier followed by an ORTEC 472A shaping amplifier with $1\ \mu\text{s}$ shaping time.

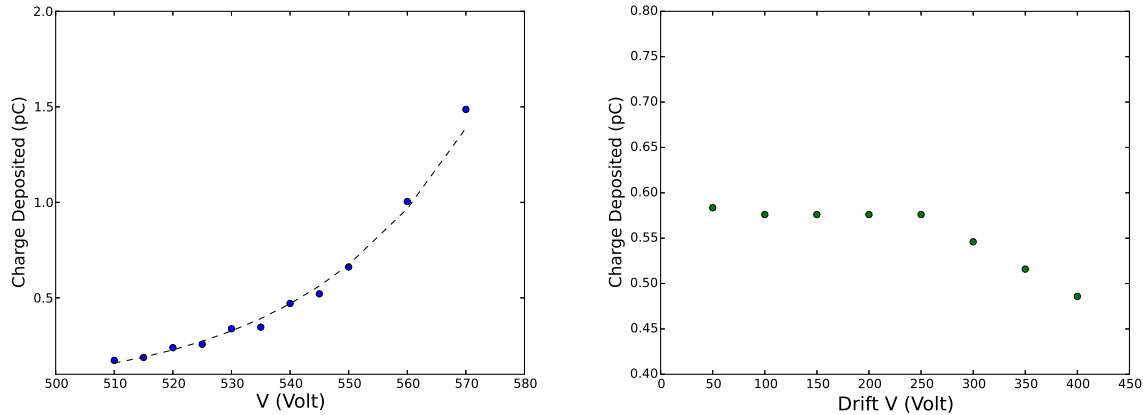


Figure 4: Dependence of the ^{55}Fe 6 KeV peak on the anode (left) and drift (right) voltage.

4 The VMM1 readout

In these measurements, we use two VMM1 chips covering the central 5.12 centimetres of the micromega. In the following, we use the convention that the number of the 128 strips increases with increasing y value. The FE-mini1 board hosting the first 64 strips is referred to as board-0 or board-16, whereas the next is referred to as board-1 or board-17. The functionality of the VMM1 is detailed in Ref. [8]. For each channel, the ASIC chip contains an analog section with a selectable-gain charge preamplifier and a high-order DDF (Delayed Dissipative Feedback) shaper with a peaktimes selectable from 25 to 200 ns². We use the largest gain of the charge amplifier (9 mV/fC) because a significant fraction of MIP signals is close to the discriminator threshold. We study the chip performance using 50, 100 and 200 ns peaktimes.

The shaping amplifier is followed by a discriminator with a threshold value common to all channels. The possibility is provided to adjust individually the threshold of each channel with a full range of 15 mV. As is well known, this fine adjustment is at the moment insufficient [3].

The output of the shaping amplifier is followed by a peak detector – armed by the discriminator – the voltage output of which, referred to as the PDO, is stored until digitized. The option is available for any channel over threshold to enable the acquisition of its neighbor channels. However, we find that the arrival time of neighbor-enabled signals is likely compromised by cross-talk in the chip, and this study does not use this option.

The detection of a peak starts the TAC ramp for this channel. All TAC ramps are stopped by the cosmic-ray trigger. The scale of the TAC ramp is selectable and we use the 1000 ns scale, also referred to as 1 mV/1 ns. The TAC voltage, referred to as TDO, is also stored until read out together with the PDO and the channel address. Upon a trigger arrival, the stored PDO and TDO values are multiplexed to the BNL CDAQ card where they are digitized and transmitted together with the address of the channel. Data are recorded with a QT-based program [7]. We have not yet studied directly the performance of the ART signal, but we get a feeling of it, when generated at peak-finding, by looking at the time distribution of the earliest TDO signal in both FE boards.

4.1 VMM1 calibration

The VMM1 chip offers the possibility of calibrating the gain and pedestal of the PDO and TDO values. This is achieved by enabling a 1.2 pF test capacitor for each channel. A voltage step, controlled by the onboard pulser DAC and test clock, is sent to any combination of enabled channels. We measure the PDO pedestals and gains (mV/fC) of all 128 channels, one at a time, by using voltage steps generated with different DAC values (from 250 to 400 in steps of 50). As is well known, voltage steps do not correspond exactly to the DAC values and have been measured with an oscilloscope using the monitor channel. The relationship between DAC value and step voltage is quite different for the two chips. Figure 5 shows the calibration of the DAC pulse on each VMM1 chip. In the Atlas experiment, each DAC output will have to be measured with accurate digitizers or the calibration will be a never ending loop.

The TDO values have been calibrated using DAC=400 step pulses and delaying the TAC stop by 250, 500, 750 and 1000 ns with respect to the injected-pulse time. Figures 6, 7 and 8 show intercepts and slopes of the time and charge calibration for each of the 128 VMM1 channels. We have calibrated one channel at a time because it is well known by now that the leakage rate of the VMM1 multiplexer can be as large as 1.0 mV/ μ s, and the calibration would depend on the number of channels fired at the same time. To mitigate this problem, we digitize only once the TDO and PDO values of each channel. For data events with more than one strip signal in each ASIC, we correct for the measured leakage rate as detailed in Ref. [3].

² The analog output of the shaping amplifiers can be monitored one channel at the time.

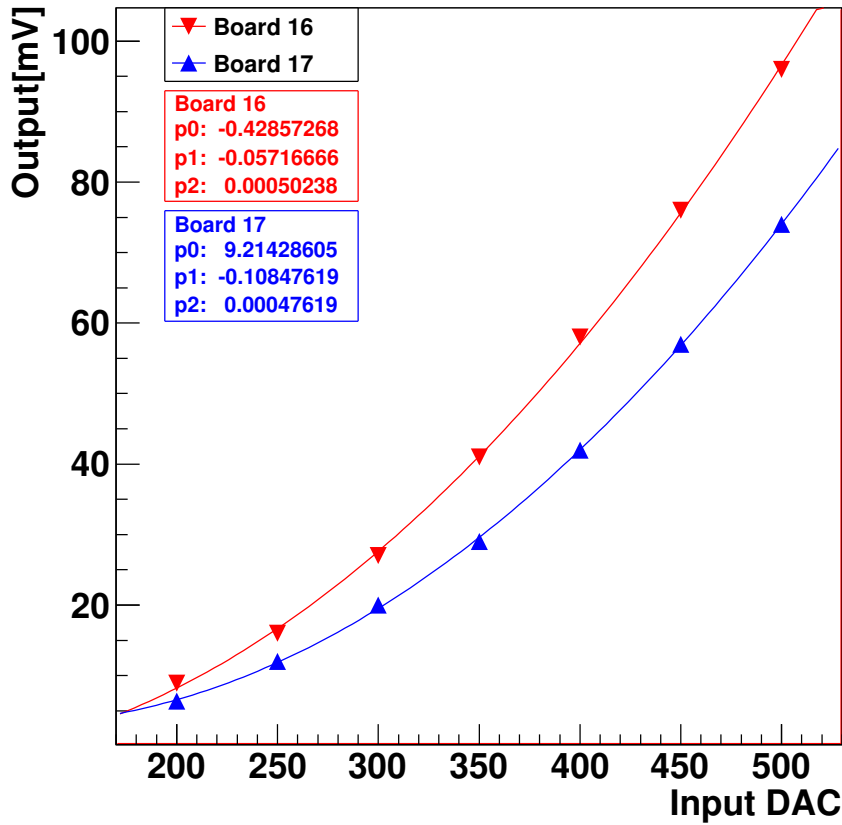


Figure 5: Calibration of the test pulse DAC of each of the two VMM1 chips. The lines and statistics insert show a quadratic fit to each set of points.

4.2 VMM1 thresholds

The same DAC value of 250 sets the common discriminator threshold at 258 and 215 mV in board-16 and board-17, respectively. As seen in the previous figures, pedestals are also quite different. Therefore, we have set the threshold of each channel by using data to equalize the minimum charge detected by each strip. The best equalization is shown in Fig. 9. It is obvious that there are signals close to the threshold and likely below it.

4.3 Neighbor channel enable

Therefore, it seemed a good idea to use the neighbor-enable option to recover signals under threshold. Figures 10 show the TDO distribution for each channel in 50000 muon events acquired using or not-using the neighbor-enable option. One sees that channels rescued as neighbor arrive approximately 100-150 ns earlier than channels above threshold. Since, as we will see later, the electronic noise is negligible, this effect has to be caused by cross-talk inside the ASIC. In any event, we decided not to use this option in the remaining of our study.

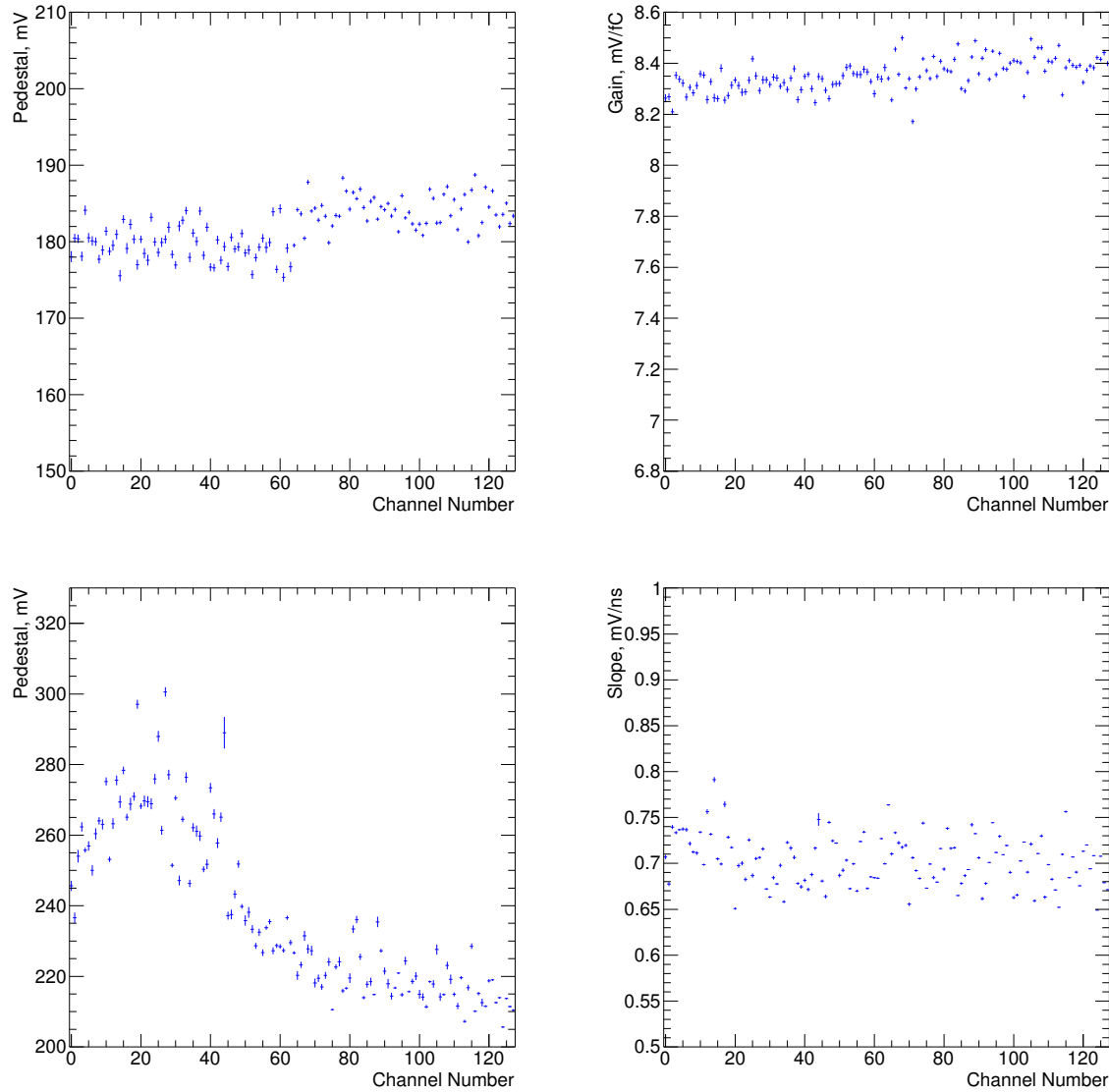


Figure 6: Results of the calibration of the two VMM1 chips when using a peaktime of 200 ns. Pedestals (top left) and Gains (top right) of the charge calibration. Pedestals (bottom left) and Slopes (bottom right) of the time calibration.

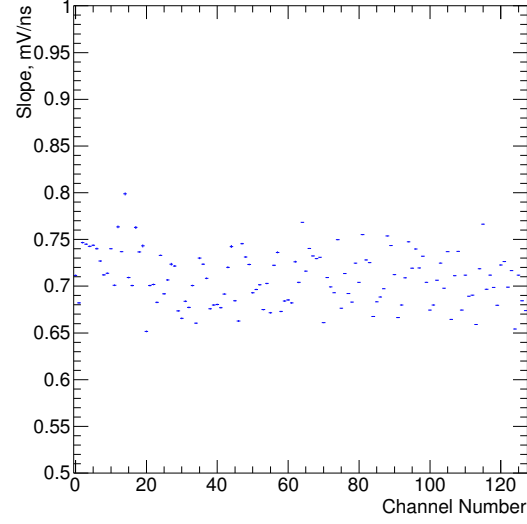
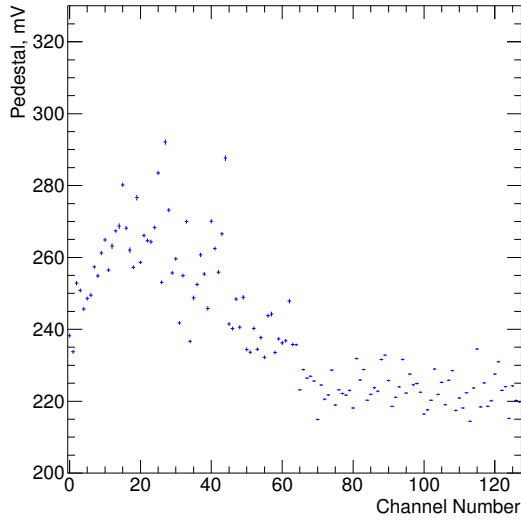
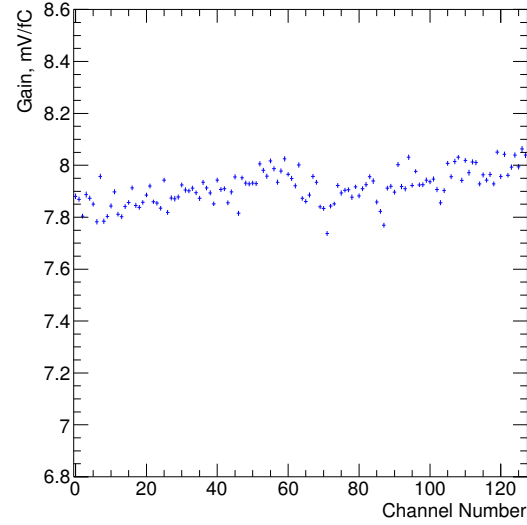
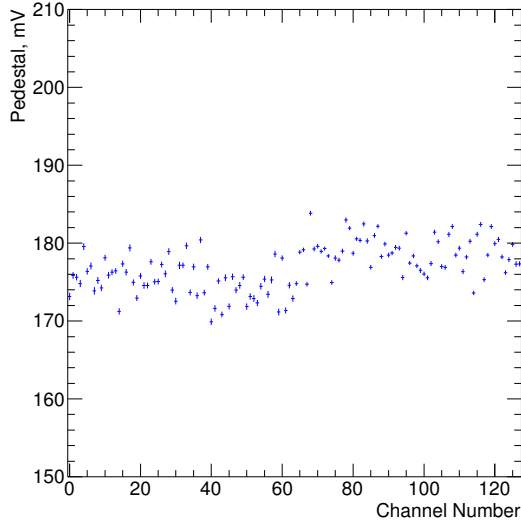


Figure 7: Results of the calibration of the two VMM1 chips, using a peaktime of 100 ns. Pedestals (top left) and Gains (top right) of the charge calibration. Pedestals (bottom left) and Slopes (bottom right) from time calibration.

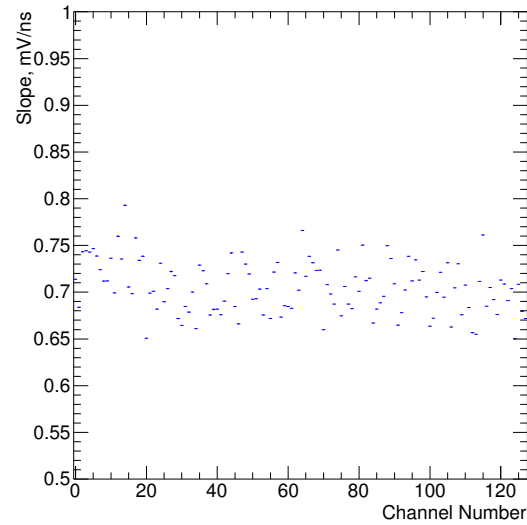
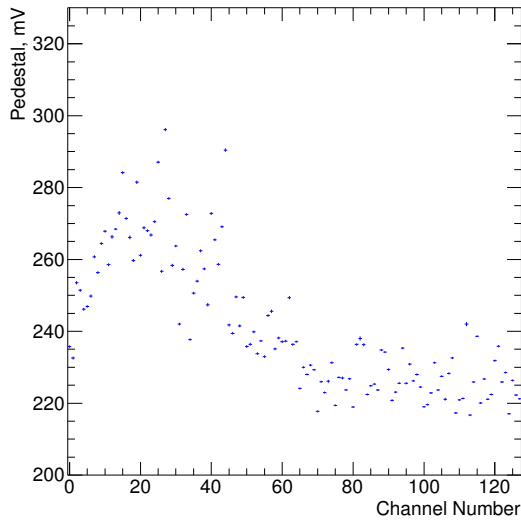
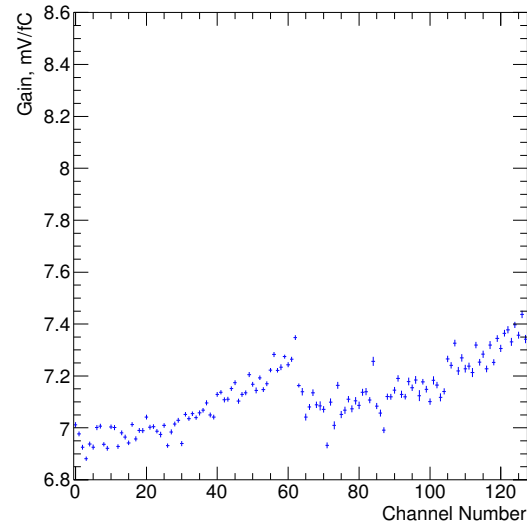
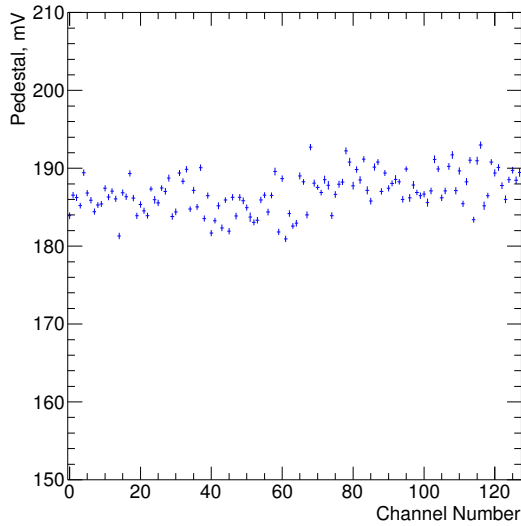


Figure 8: Results of the calibration of the two VMM1 chips, using a peaktime of 50 ns. Pedestals (top left) and Gains (top right) of the charge calibration. Pedestals (bottom left) and Slopes (bottom right) from time calibration.

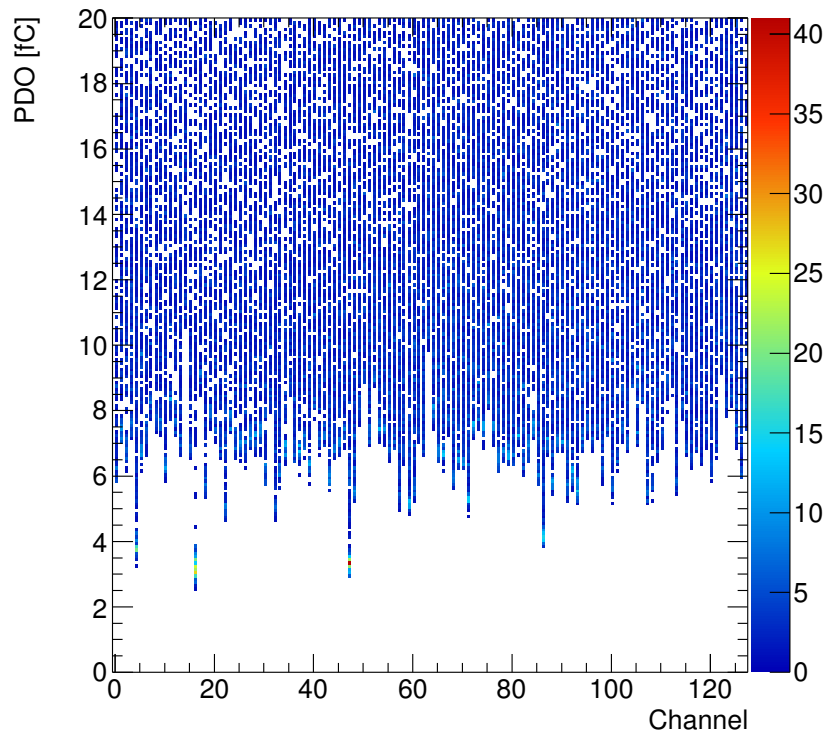


Figure 9: Charge deposited in each strip by 10^5 muons after a series of coarse and vernier threshold adjustments.

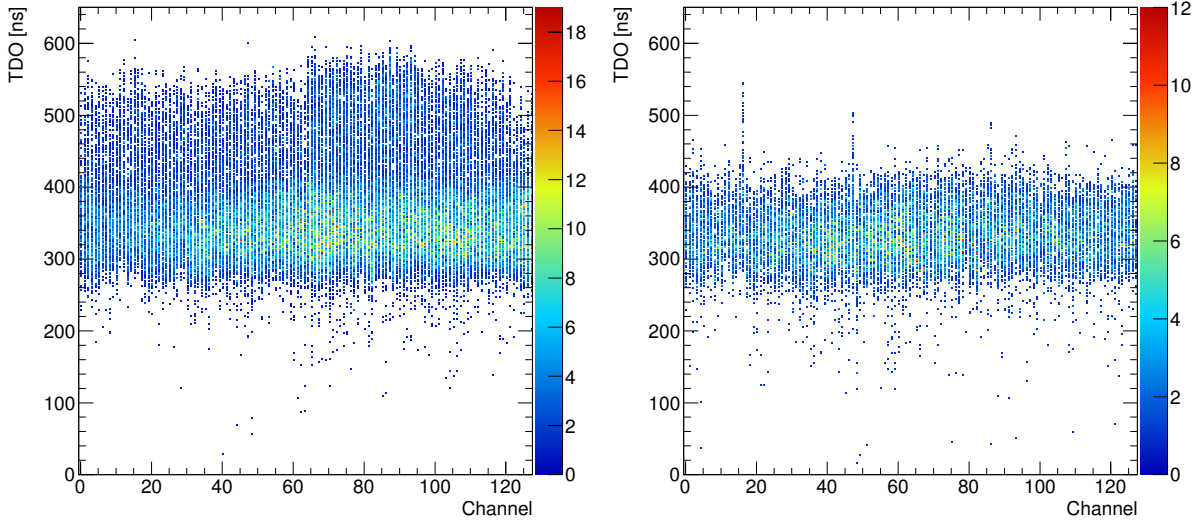


Figure 10: Distributions of TDO values for each channel in 10^5 muon events acquired using (left) and not using (right) the neighbor-enable option. The TDO value is the time difference between the micromega signal at peak and the cosmic trigger. Larger TDO values correspond to earlier signals.

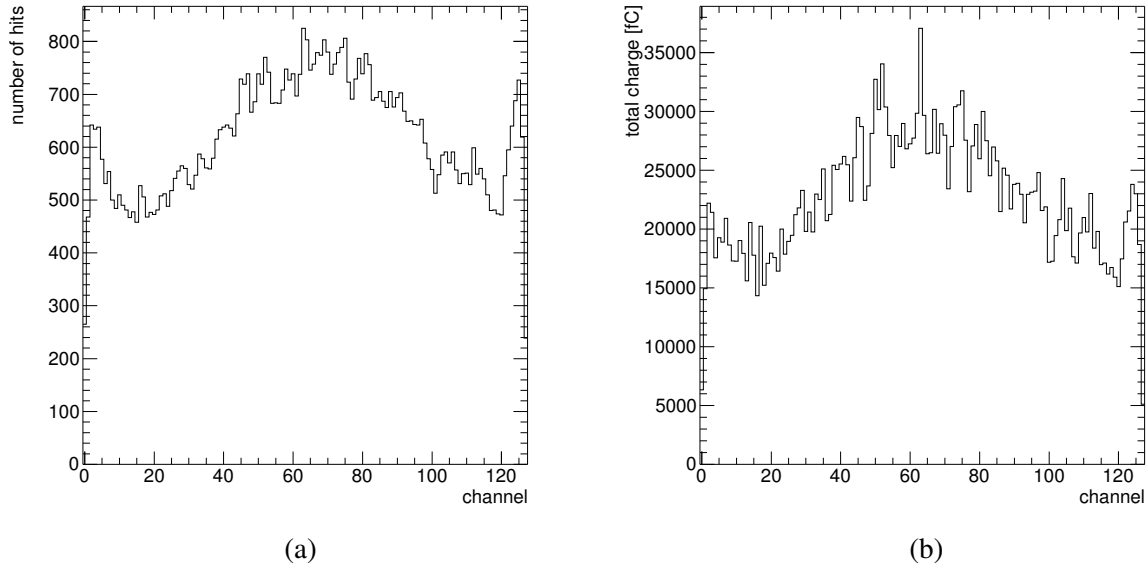


Figure 11: Distribution of the number of hits (a) and deposited charge (b) in the 128 channels of the micromega readout for 25634 muon events, using a peaktimes 200 ns and an anode voltage of 550 V.

5 Micromega response to cosmic muons

Figure 11 shows the number of hits and the total deposited charge for each readout strip in a run using a peaktimes of 200 ns and an anode voltage of 550 V. The data set contains 86462 events with only one muon, 25634 of which leave a signal in the micromega detector³. The increase of counting rate and deposited charge in the first and last eight channels is due to muons passing close to but outside of the micromega area being readout. In some cases, we exclude clusters the barycenter of which lies in this region (fiducial cut, referred to as FD cut).

We use a simple cluster algorithm, referred to as *pacman* clustering, to reconstruct the muon position and arrival time using the readout strip signals. We sort all the hits according to their global strip number from 1 to 128. The clustering starts from the lowest strip with charge above 6 fC (seed). We then add to the cluster strips with higher strip number if their charge is larger than 2.5 fC and their arrival time is within the expected time window with the condition that their distance is smaller than or equal to five strips. Each time we add a strip, we update the end of the cluster, the total charge and the average arrival time. The same search is repeated from the last included strip. The same search is then extended backward starting from the seed strip. Strips not included in the first cluster are searched again for additional clusters. This algorithm reconstructs a cluster in 25589 events, 99.8% of all events with some deposited charge above threshold. The number of events with more than one cluster is about 3%, and to make life simple we use only the cluster with the highest charge unless specifically noted.

Figure 12 shows the charge distribution of reconstructed clusters. One notes that the charge integrated by board-16 is larger than that of board-17. This happens because its effective peaktimes is larger. This difference cannot be detected during calibrations because, in contrast with micromega signals, step pulses have a risetime much smaller than the peaktimes of the charge integrator. Accordingly, it will be shown later that TDO values generated at peak-found are smaller in board-16.

³ Because the effective area of the SP counter is difficult to assess, the fraction of events with a micromega signal cannot be translated into an efficiency measurement. However, this fraction will be used to monitor the dependence of the micromega efficiency on voltages and peaktimes.

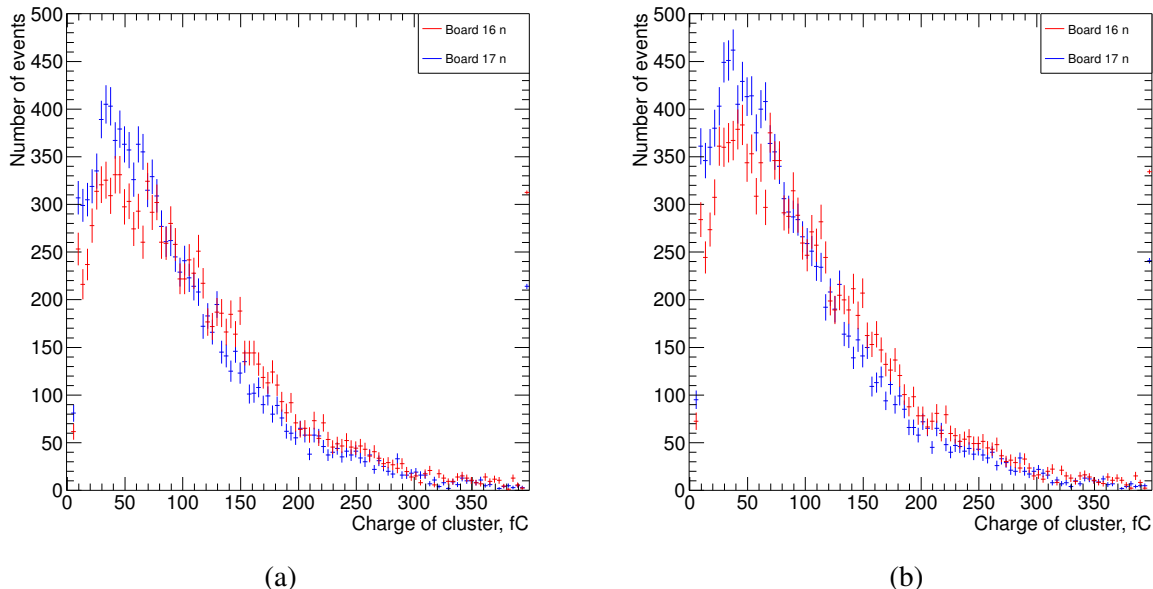


Figure 12: Distribution of the charge of clusters reconstructed in board-16 and -17 with (a) and without (b) FD cut (see text), using a peaktme of 200 ns and an anode voltage of 550 V. Distributions are normalized to the same number of events.

In the study of Ref [3], by using the 6 KeV line of ^{55}Fe decays we have measured that the charge integrated by the VMM1 with a 200 ns peaktme is approximately one half of that collected by a single ORTEC preamp+amp system with a 1 μs shaping time connected to all readout strips. In this measurement, we can only compare the wide charge distribution of the muon clusters above threshold integrated by the VMM1 to the narrow charge distribution of the 6 KeV line integrated with the ORTEC system. The average muon charge is approximately 100 fC, or 1/6 of the charge corresponding to the 6 KeV peak integrated by the ORTEC system (see Section 3) ⁴. However, the most probable integrated charge is approximately 50 fC. In the end, the only relevant information is the measured distribution of the muon charge integrated by the VMM1 shown in Fig. 12.

One also notes that the charge distribution is close to the threshold which makes it difficult to assess the micromega efficiency with the present setup. As shown by Fig. 13, the small charge clusters are those with low strip multiplicity.

Figure 14 shows the distribution of the number of strips in reconstructed clusters. It also shows that all strips in a cluster are contiguous in more than 90% of the cases. Figure 15 shows the average charge of a cluster as a function of the number of strips in the cluster. In 98% of the clusters, i.e. those with ≤ 5 strips, the number of strips is linearly proportional to the collected charge. This is somewhat at odds with the popular model in which the strip multiplicity depends on the angle of incidence of a track. If this were the case, the average charge would be almost independent of the cluster multiplicity. This observation fits better a model in which: a) the drift of ions in the amplifying gap builds a difference of potential $\delta V(t)$ on the resistive anode; b) the strip signals arise from the capacitive couplings between the resistive anode and the readout strips; c) the larger is $\delta V(t)$, the larger is the number of strips with an induced signal above threshold. This raises a concern on the possible use of micromegas equipped with VMM readout as μ TPC detectors, which is further investigated in Sects. 5.5 and 6.

⁴The MIP ionization loss in 5 mm of gas is approximately 1 KeV.

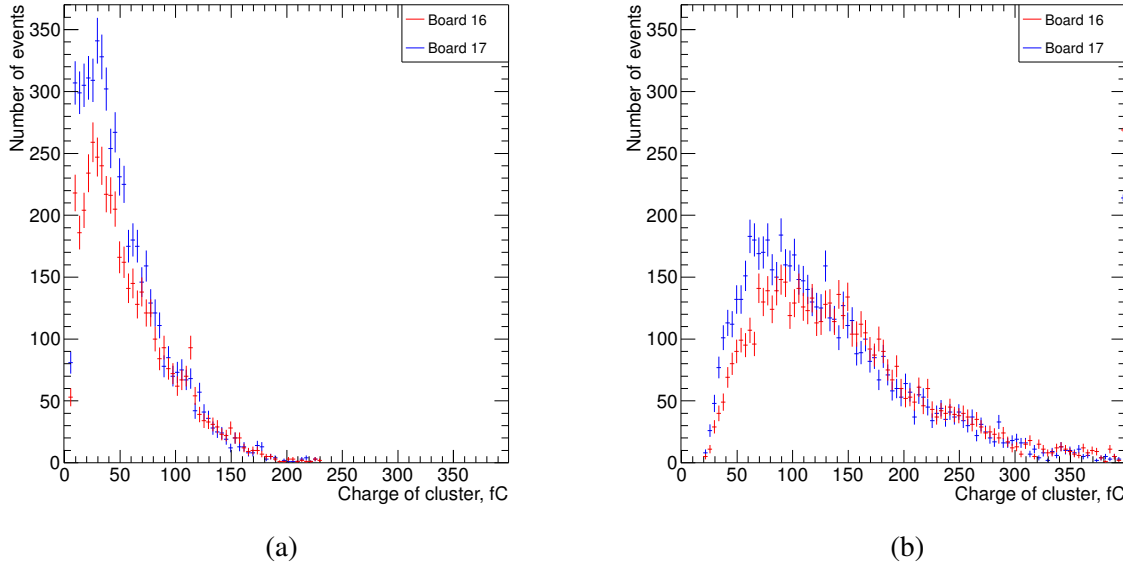


Figure 13: Charge distributions of clusters consisting of (a) ≤ 2 and (b) ≥ 3 strips, using a peaktimes of 200 ns and an anode voltage of 550 V. The FD cut has been applied.

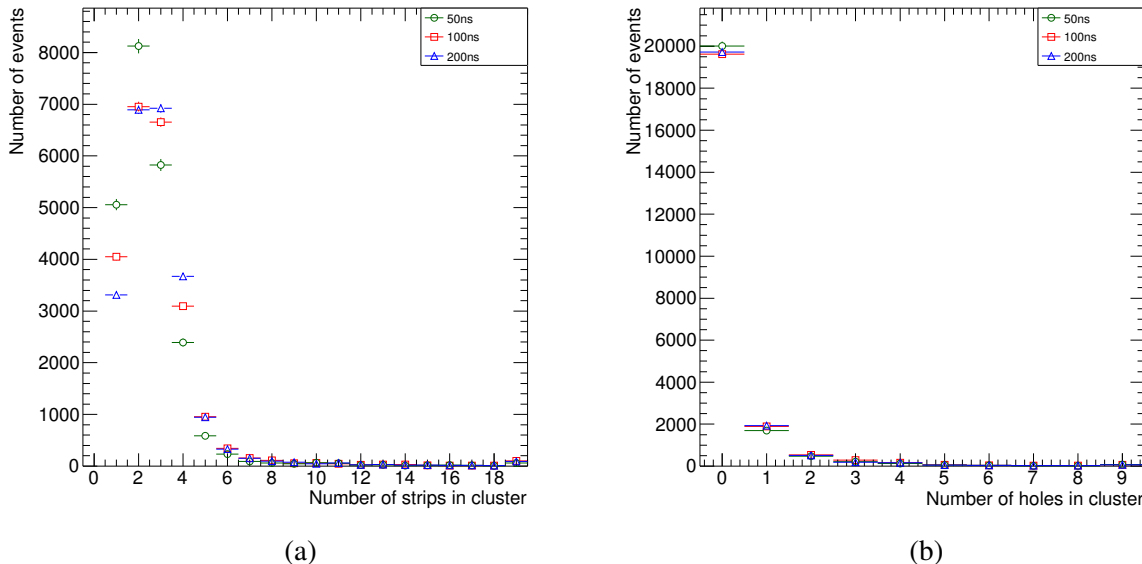


Figure 14: Distributions of (a) the number of strips in a cluster and (b) of the number of missing channels inside a cluster, using an anode voltage of 550 V and peaktimes of 50, 100, and 200 ns. The FD cut is applied.

5.1 Measurement of the electronic noise

We have investigated if signals close to the VMM threshold are due to electronic noise by moving the SP counter to the side of the micromega. The fraction of muon events with a micromega cluster above threshold decreases from 29.6% to 0.07%. The distribution of the cluster charge for the same number of muon triggers is compared in Fig. 16. It is our conclusion that the signals close to the threshold are due to real muons and the electronic noise is negligible.

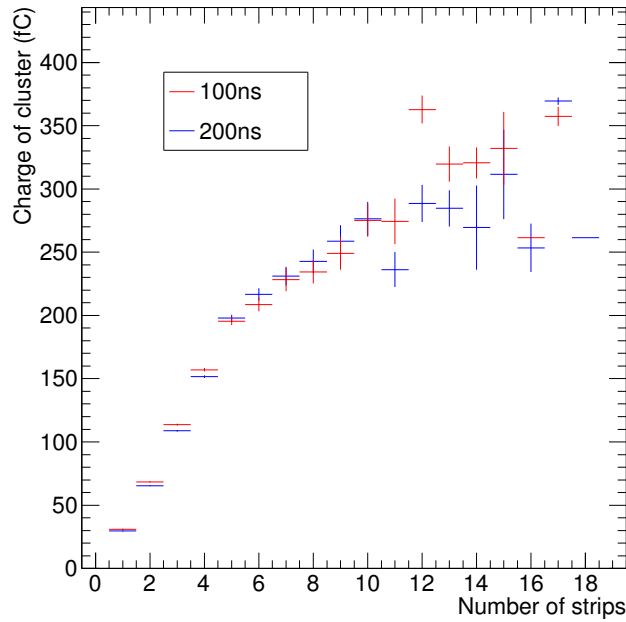


Figure 15: Average charge of clusters as a function of their strip multiplicity, using an anode voltage of 550 V and peaktimes of 100 and 200 ns.

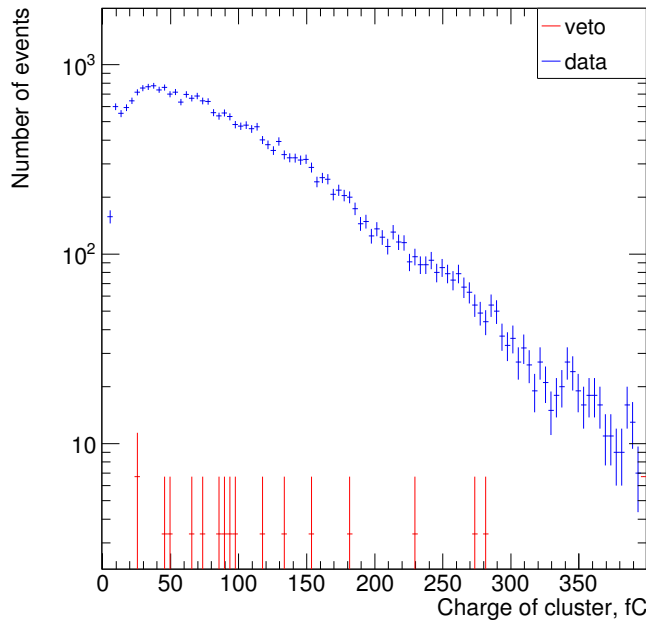


Figure 16: Distributions of cluster charges for muon events triggered with the SP counter on top (blue points) and to the side (red points) of the micromega. Distributions are normalized to the same number of muon triggers.

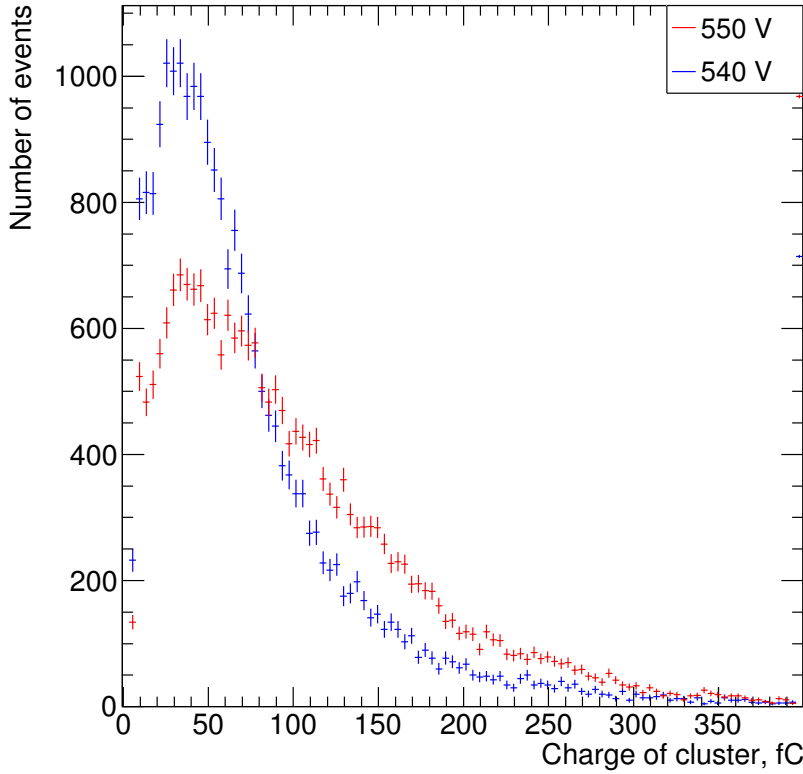


Figure 17: Distributions of the cluster charge for anode voltages of 540 and 550 V, using a peaktimes 200 ns. The FD cut is applied. Distributions are normalized to the same number of events.

5.2 Dependence of the collected charge on the voltage of the resistive anode

Figure 17 compares distributions of cluster charges when lowering the anode voltage from 550 to 540 V. The ratio of the averages of the cluster charge distributions is 72%, in reasonable agreement with the 68% expected from Fig. 4. However, the ratio of the number of reconstructed clusters normalized to the same numbers of muon triggers at 540 and 550 V is 1.007 ± 0.010 . In conclusion, at 550 V the micromega efficiency is definitely in plateau.

5.3 Comparison between 200, 100, and 50 ns peaktimes

For triggering reasons, a shorter peaktimes is often advocated. Using the 100 ns peaktimes, we have collected 75874 muons events in which 20504 events have some micromega signal and in which 20476 events have at least one cluster. It follows that the micromega efficiency at 550 V drops by 8.9% when shortening the peaktimes by 100 ns. We have also collected 42476 events using a peaktimes of 50 ns. In these events, 10905 events contain some micromega signal and 10799 events contain at least one cluster. It follows that, when shortening the peaktimes by 150 ns, the micromega relative efficiency drops by 15%. Figure 18 compares the cluster-charge distributions for different peaktimes.

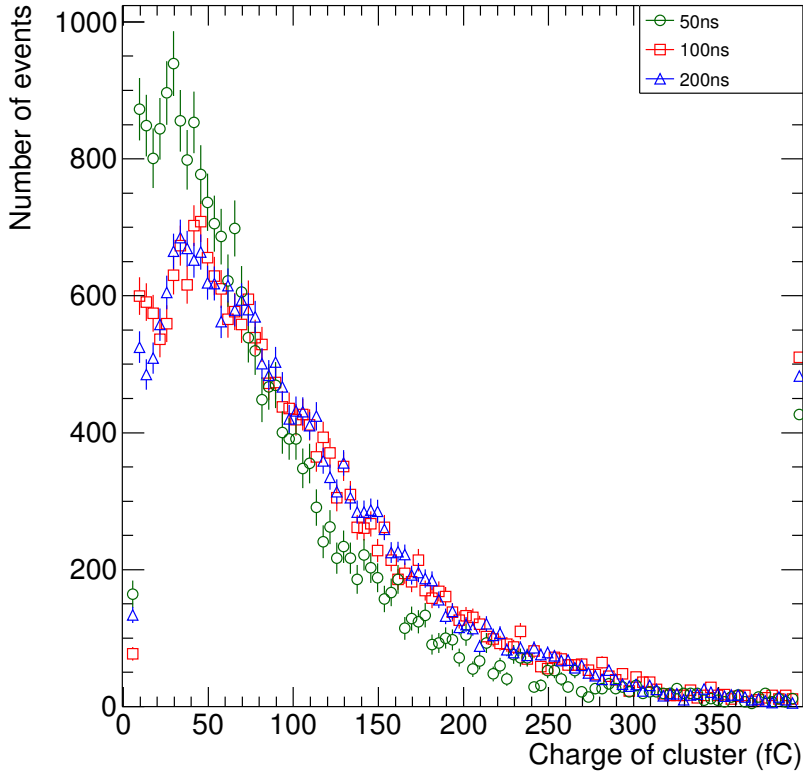


Figure 18: Distributions of the cluster charge using peaktimes of 50, 100, and 200 ns and an anode voltage of 550 V. Distributions are normalized to the same number of clusters. The micromega efficiency drops by 8.9% when going from 200 to 100 ns peaktimes, and by 15% when going from 200 to 50 ns. The FD cut is applied.

5.4 Arrival times of micromega signals

This subsection is dedicated to the accuracy of the VMM1 TDO values, defined as the time difference between an integrated micromega signal at peak and the SP signal which has an accuracy of 1.2 ns. Figure 19 shows the TDO distributions for all channels in one VMM1 board. It can be compared with Fig. 23 of Ref. [11]. When forming a cluster, we also average the TDO's of all strips belonging to the cluster, referred to as cluster-TDO. Independently of cluster finding, for every event we also calculate the largest, referred to as earliest-TDO, TDO value in the two VMM1 chips. This emulates the arrival time of the ART signal used by the micromega trigger.

Figure 20 shows the mean of the cluster-TDO's as a function of the cluster charge as well as the time distribution of all TDO's and earliest-TDO's for all channels. As mentioned earlier, board-16 has a longer peaktimes and the cluster-TDO's arrive approximately 5 ns later. There is a small slewing of the arrival time as a function of the cluster charge, the slope of which is approximately 0.06 – 0.09 ns/fC. This slewing time is appreciable but negligible with respect to the RMS of the distribution of the cluster-TDO's shown in Fig. 21. This figure also shows the distribution of the earliest-TDO's in the event. One sees that the time jitter (full width) of the earliest-TDO covers at least 8 LHC bunches. This latter distribution is difficult to reconcile with that of the earliest arrival time based on a direct study of the ART signal [9] [5, fig. 5.9] unless the CDAQ card or the VMM1 chip introduce a random time jitter of the order of 100-150 ns between the cosmic trigger and the TAC stop. Figure 22 shows the earliest-TDO distributions for different track angles. Tracks with larger angles yield on average larger earliest-TDO

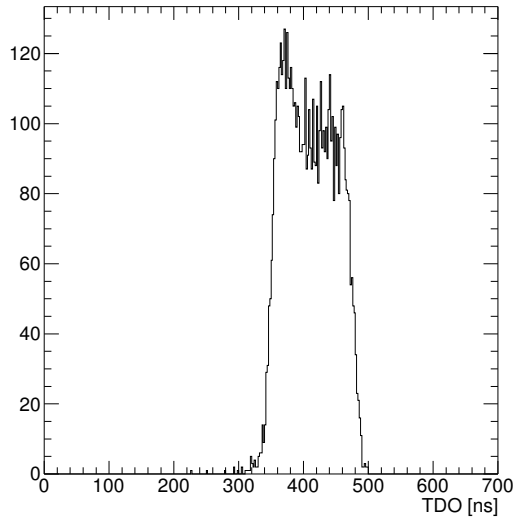


Figure 19: Time distribution for all strips in a cluster on board-17. We use tracks with angle of incidence $\geq 20^\circ$, 100 ns peaktime, and an anode voltage of 550 V.

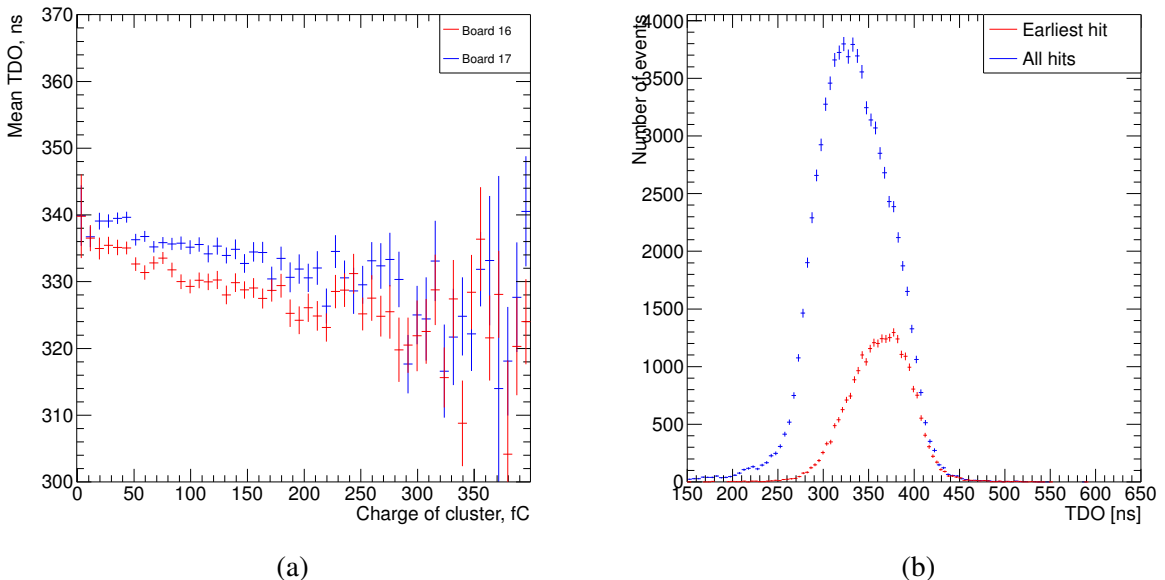


Figure 20: (a): Mean of all cluster-TDO values as a function of the cluster charge for both VMM1 chips using a peaktime of 200 ns. The anode voltage is 550 V. (b): Time distributions of all TDO and earliest-TDO values for all readout strips using the same settings.

values, but the overall time jitter ($\simeq 200$ ns) is independent of the track's angle. The fact that the shape of earliest-TDO distribution depends on the track angle does not support the above-mentioned hypothesis that the width of the distribution is due to random jitter of the TAC stop in the VMM1 chip. We are presently adding the ART signals to our data acquisition system, and will revisit the issue in a not so distant future. For now, the most likely explanation of the difference is that the study in Ref. [9] was not acquiring the earliest 100-120 ns of the PDO time distribution. If we are correct, the micromega trigger will have to be formed over 8 LHC bunches, and not 2-3 as advertised in the NSW TDR [5]. The addition of 120 ns to include all micromega earliest hits will exceed the $1\ \mu\text{s}$ time budget allocated to the micromega trigger.

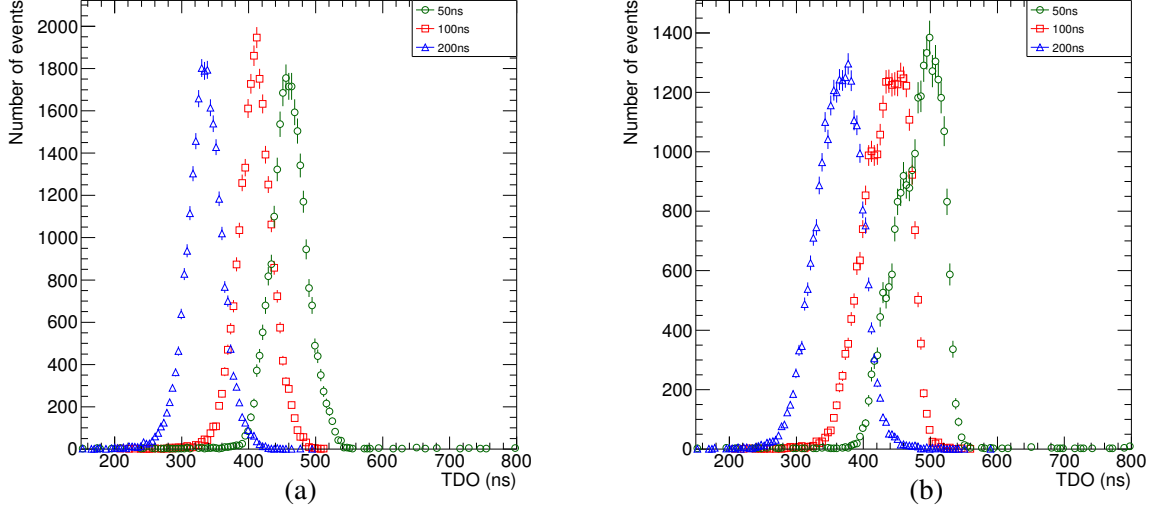


Figure 21: Distributions of (a) the cluster-TDO and (b) earliest-TDO using peaktimes of 50, 100, and 200 ns and an anode voltage of 550 V. Distributions are normalized to the same number of events.

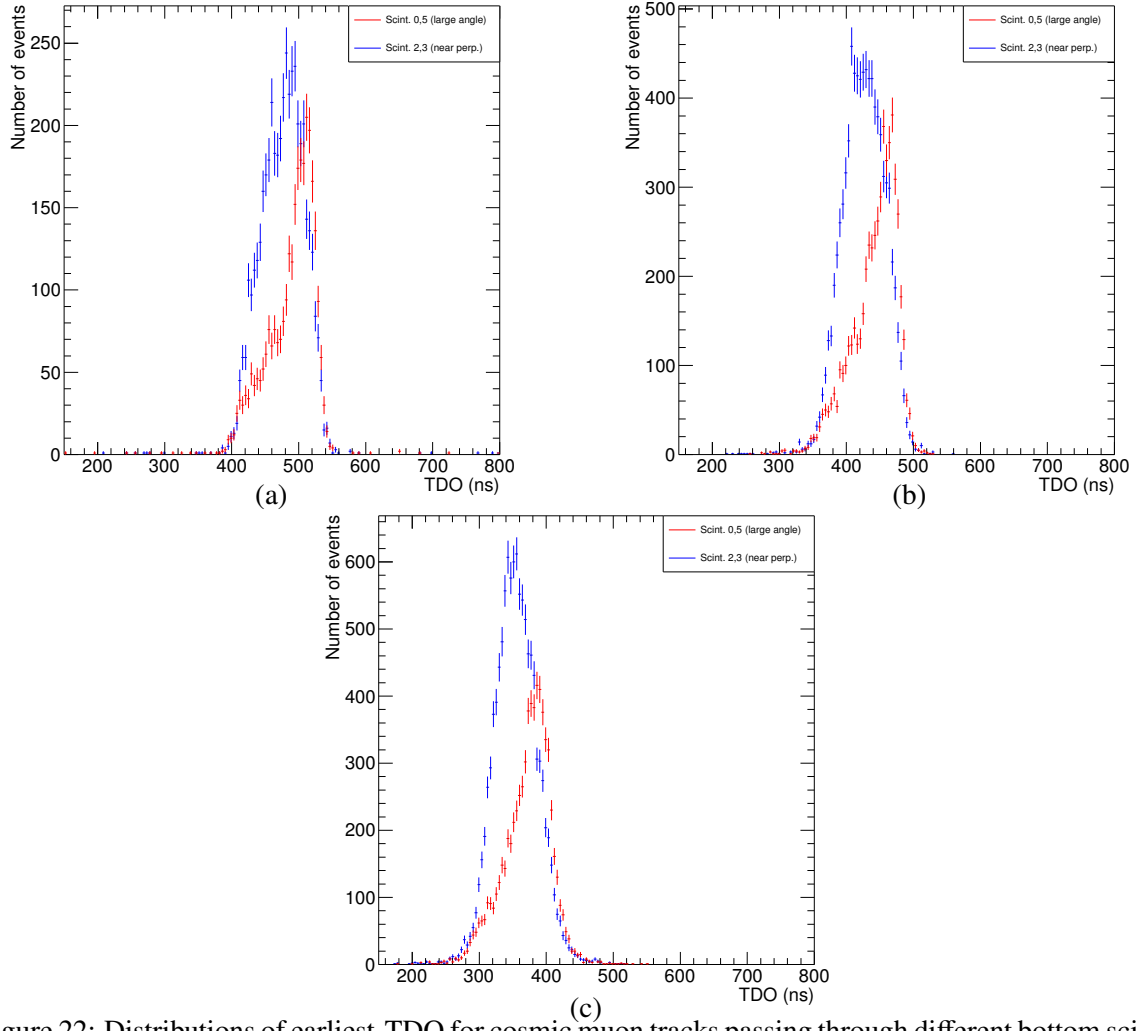


Figure 22: Distributions of earliest-TDO for cosmic muon tracks passing through different bottom scintillators, using peaktimes of (a) 50 ns, (b) 100 ns, and (c) 200 ns and an anode voltage of 550 V. Scintillators 0,5 (red points) select tracks with $11^\circ - 16^\circ$ angles in the $y-z$ plane, whereas scintillators 2,3 (blue points) select tracks with $0^\circ - 5^\circ$ angles.

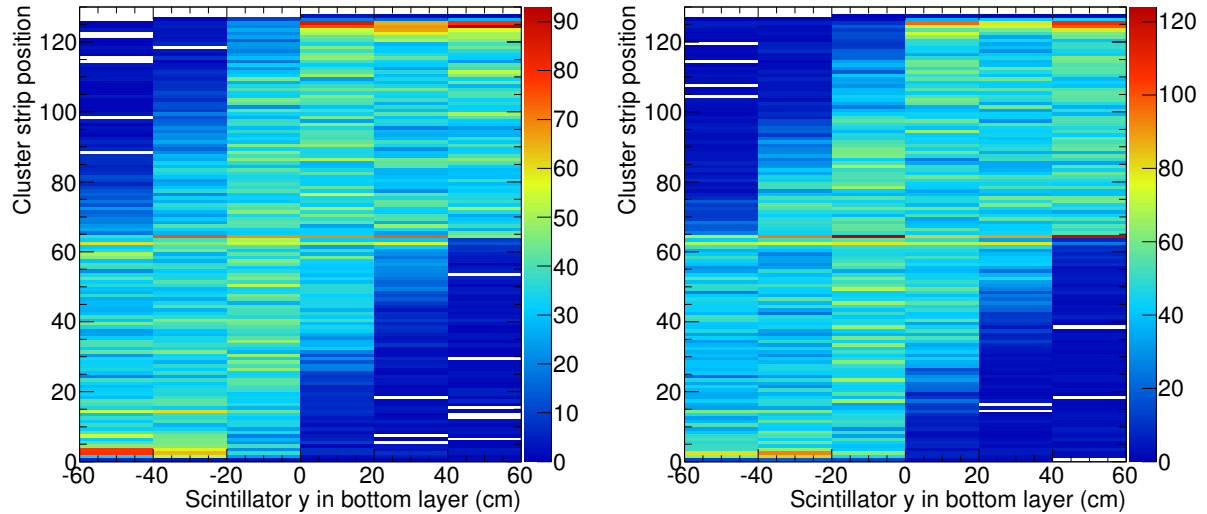


Figure 23: Dependence of the cluster y coordinate (measured in strip number) on y -trigger (see text) for (left) 100 ns and (right) 200 ns peaktimes. The anode voltage is 550 V. The FD cut is applied.

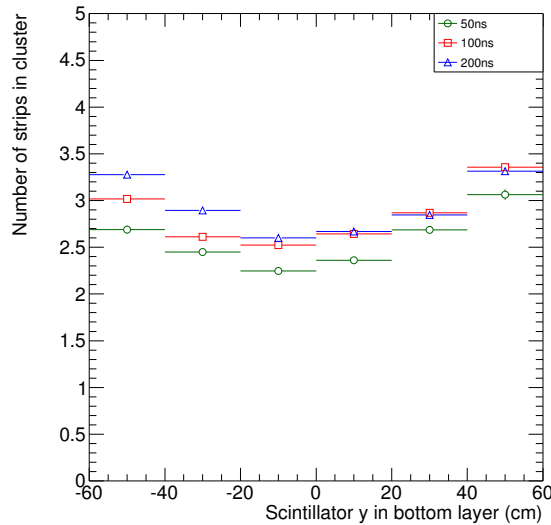


Figure 24: Average multiplicity of clusters as function of y -trigger for 50, 100, and 200 ns peaktimes and an anode voltage of 550 V. The FD cut is applied.

5.5 Micromega response to the muon angle of incidence

We study the micromega response as a function of the muon angle of incidence by selecting muons triggered by different bottom scintillators with y coordinates ranging from -60 to $+60$ cm in steps of 20 cm. By requesting scintillator hits with increasing y coordinate, we change the muon angle in the $y - z$ plane, orthogonal to the direction of the micromega readout strips, from -13° to 13° in six steps of 5° , each with an RMS of 1.5° . Figure 23 shows the y position of micromega clusters, measured in strip number, as a function of y -trigger, the y coordinate of the bottom counter triggering the event. Figure 24 shows the average multiplicity of a cluster as a function of y -trigger. The average multiplicity increases by 0.6 strips when the muon angle of incidence increases from 0° to 13° . Ideally, the number of strips in a cluster should increase from 1 to 3 when the incidence angle grows from 0° to 13° . This does not happen because, when the same ionization charge is shared by more strips, strip signals are smaller and more signals fall below the VMM1 threshold. Because of this, as noted earlier, the cluster multiplicity is mostly determined by the size of its charge.

6 Study of the μ TPC mode

A detailed study of the micromega performance as μ TPC [10] has shown that, when using the APV25 readout, it is possible to reconstruct angles of incidence with an accuracy of the order of 2-3°. Similar resolutions have been achieved using the VMM1 readout [11] even if, when using VMM1, the only additional information consists of the TDO value of each strip in a cluster. Puzzled by these results since the cluster multiplicity depends mostly on the cluster charge, we make use of the HCRT's quite large angular coverage to further investigate.

In 44% of the events, the cluster multiplicity is ≤ 2 and, when emulating the study in Ref. [11], we do not use this subsample. The remaining 56% of the events are dominated by multiplicity 3, in which case no hits can be excluded by using methods such as representations in Hough space [11]. We convert the TDO value of a strip with x coordinate into a distance $z(x)$ assuming that the drift velocity of electrons is 1 mm/20 ns. For clusters with three or more strips, we fit the $z(x)$ values as a function of the strip x position with a straight line $z(x) = x \tan \alpha + C$, where α is the angle between the track and the horizontal plane. In μ TPC mode the x position of the cluster is derived as $x_{\text{clu}} = (2.5 - C) / \tan \alpha$ (mm). However, the study of the μ TPC mode using VMM1 electronics [11] has measured the resolution of the reconstructed angle θ between the track and the vertical direction. In order to compare, we convert the slope $\tan \alpha$ into an angle θ . Using this convention, a nil slope (all hits at the same time) yields an incidence angle $\theta = 90^\circ$.

Figure 25 shows the dependence of the angle of incidence θ reconstructed in μ TPC mode on y -trigger. The angular resolution is approximately 25° for tracks with angles of incidence as large as 13°⁵.

6.1 Study of tracks with angle of incidence as large as 25°

To investigate larger angle of incidence, the center of the micromega detector and of the SP counter is moved from $y = 0$ to $y = -50$ cm. By requesting hits in bottom scintillators with increasing y -coordinate, we select muon angles in the $y - z$ plane, orthogonal to the direction of the micromega readout strips, from 0° to 25° in six steps of 5°, each with an RMS of 1.5°. In this study we use a 100 ns peaktme and an anode voltage of 550 V. We have collected 40024 single muon events, in which we reconstruct 11321 clusters. By comparing with Sec. 5.3, the micromega relative efficiency increases from 27.0% to 28.3% as tracks with higher incidence angle ionize a thicker layer of gas. The distribution of the average strip multiplicity of reconstructed clusters is shown in Fig. 26.

Figure 27 shows the average angle θ , reconstructed in μ TPC mode, and its RMS deviation as a function of y -trigger for clusters with three or more strips and clusters with two strips only. Using ≥ 3 -strip clusters, the RMS deviation is 29° and 20° for tracks with an angle of incidence of 10° and 25°, respectively. For 2-strip clusters, the RMS angular resolution is $\approx 30^\circ$ for all track angles of incidence. In conclusion, we observe angular resolutions which are 7-10 times worse than those measured in the study of Ref. [11]. In the next subsections, we investigate possible causes for this disagreement, such as slewing time correction and RMS TDO noise, and find that their contribution is negligible. We then analyze the distributions of the reconstructed slope $\tan \alpha$ and angle θ as a function of the track angle, and show that the smaller angular resolution is achieved by ignoring some of the reconstructed angles and misinterpreting geometrical boundaries on the reconstructed-angle distributions.

6.2 Slewing time corrections

We have studied how the angular resolution in the μ TPC mode is affected by the time slewing as a function of the strip charge. We observe a dependency of the hit TDO on its PDO value, which is exponentially decaying for hits with charge smaller than 15 fC and linearly rising for integrated charges

⁵ In 20% of the cases (multiplicity larger than 3), one could possibly improve the fit result by ignoring strips yielding a bad χ^2 , but at this stage we do not see the point of showing better resolution for less than 10% of all events.

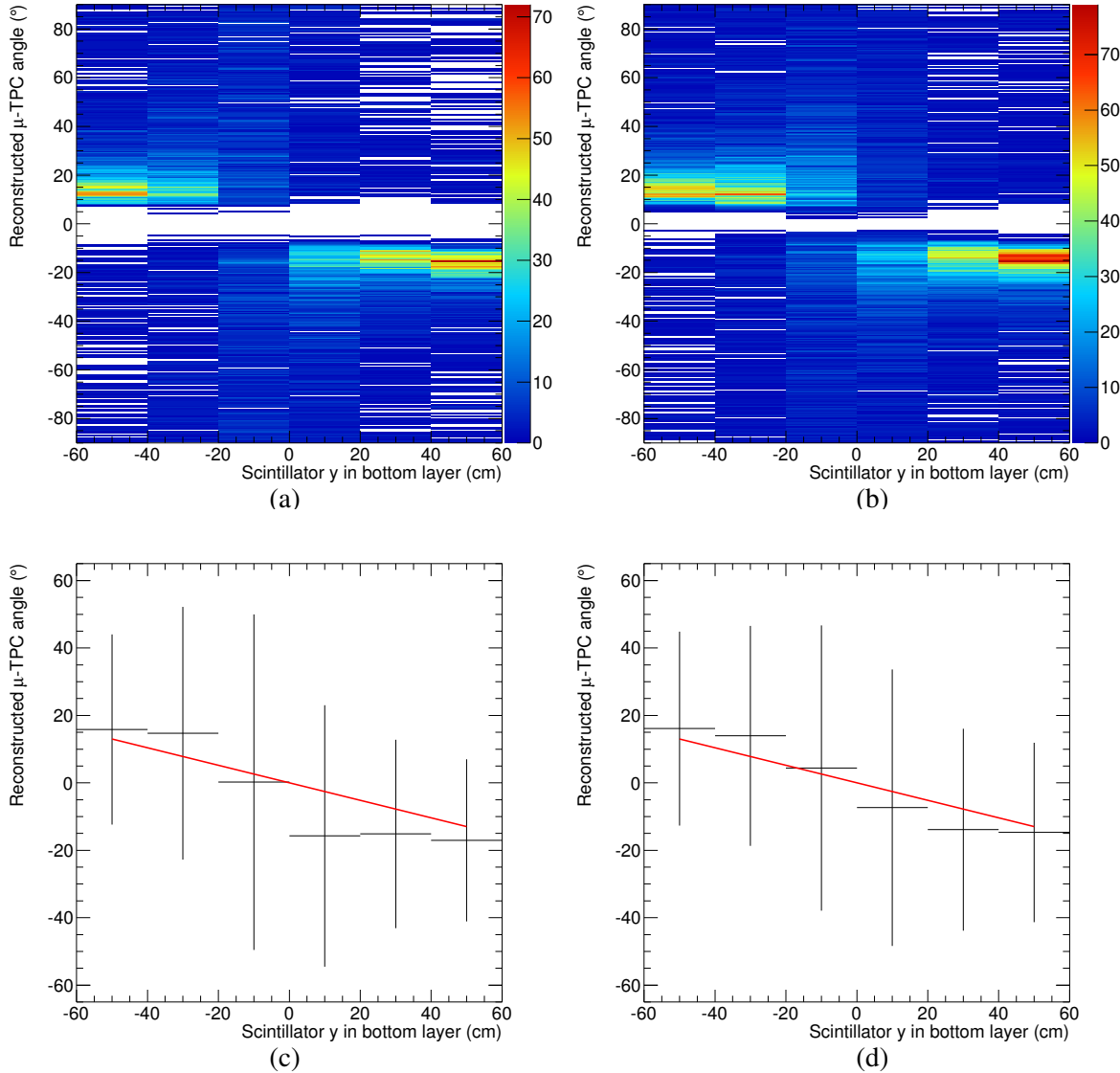


Figure 25: Distribution of reconstructed angles θ as a function of y -trigger: (a) and (c) use a 100 ns peaktimes, whereas (b) and (d) use a 200 ns peaktimes; plots (c) and (d) are x -profile histograms of (a) and (b), respectively. The error bars represent the RMS deviation. The red lines on (c) and (d) indicate the actual track angle as function of y -trigger, with a maximum angle of $\pm 13^\circ$ at $y = \mp 50$ cm. The FD cut is applied.

larger than 15 fC. We fit these distributions with an exponential function plus a straight line, and remove the fitted distribution from the data⁶. The peaktimes slewing distributions are shown in Fig. 28, before and after the correction. After correcting for the time slewing, we recalculate the average angle and its RMS deviation as a function of y -trigger, for clusters with three or more strips and clusters with two strips only. As shown by Fig. 29, analogous of Fig. 27, the angular resolution does not improve.

⁶ The exponential function has a coefficient of 71.9 (105.6) ns with a decay constant of -0.27 (-0.44)/fC, and the linear function has a slope of 0.06 (0.08) ns/fC for the 200 (100) ns peaktimes.

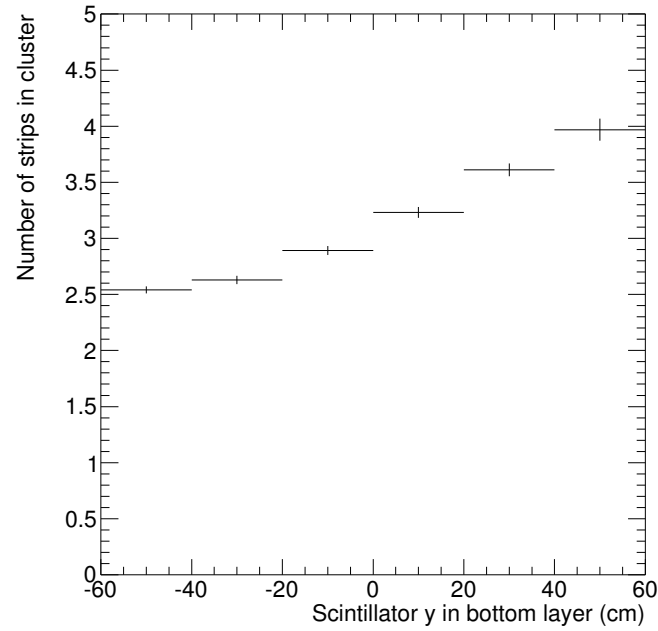


Figure 26: Average hit multiplicity of clusters as function of y -trigger using a 100 ns peaktme and an anode voltage of 550 V. The FD cut is applied.

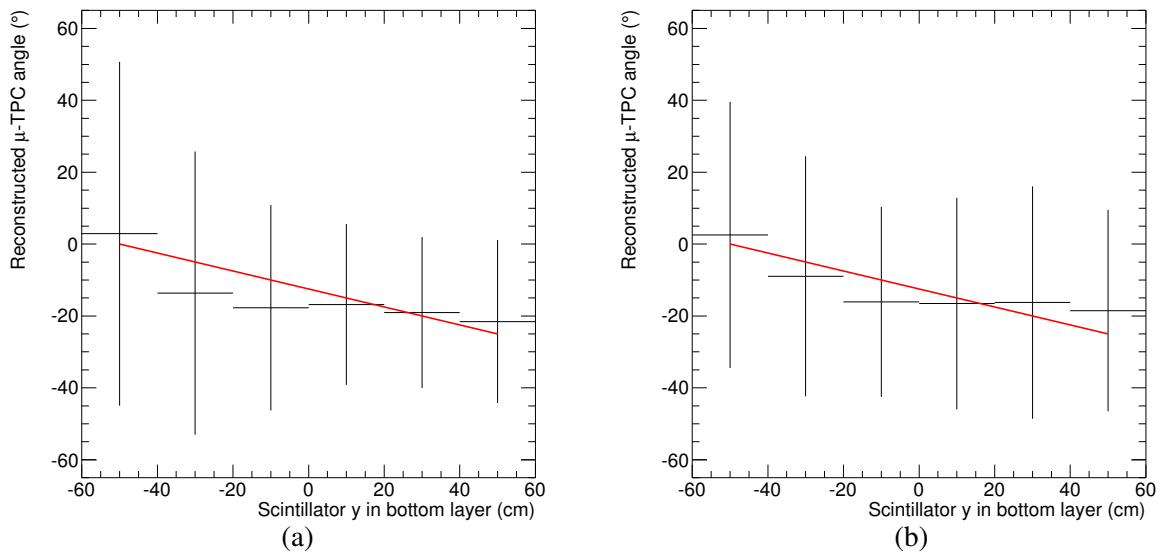


Figure 27: Average track angle θ , reconstructed in μ TPC mode, as a function of y -trigger. (a) uses only clusters with at least 3 hits, whereas (b) uses only clusters with exactly 2 hits. The red line indicates the actual track angle as function of y -trigger, ranging from 0° at $y = -50$ cm, to -25° at $y = +50$ cm. The FD cut is applied.

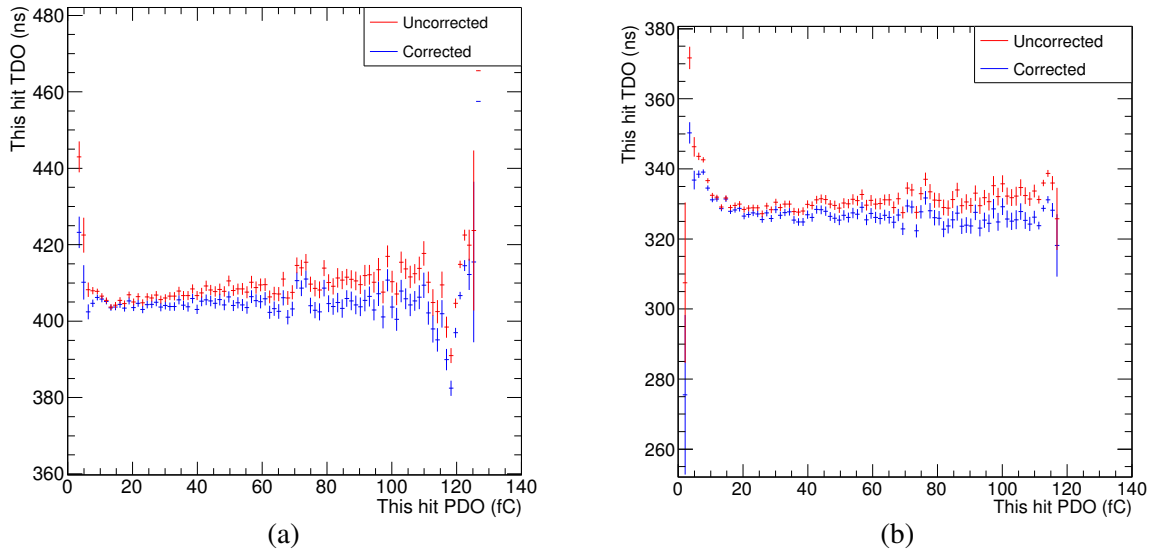


Figure 28: Average TDO of readout strips as a function of the strip PDO using (a) 100 and (b) 200 ns peaktimes. Only strips belonging to a cluster are selected. Slewing-corrected distributions are also shown.

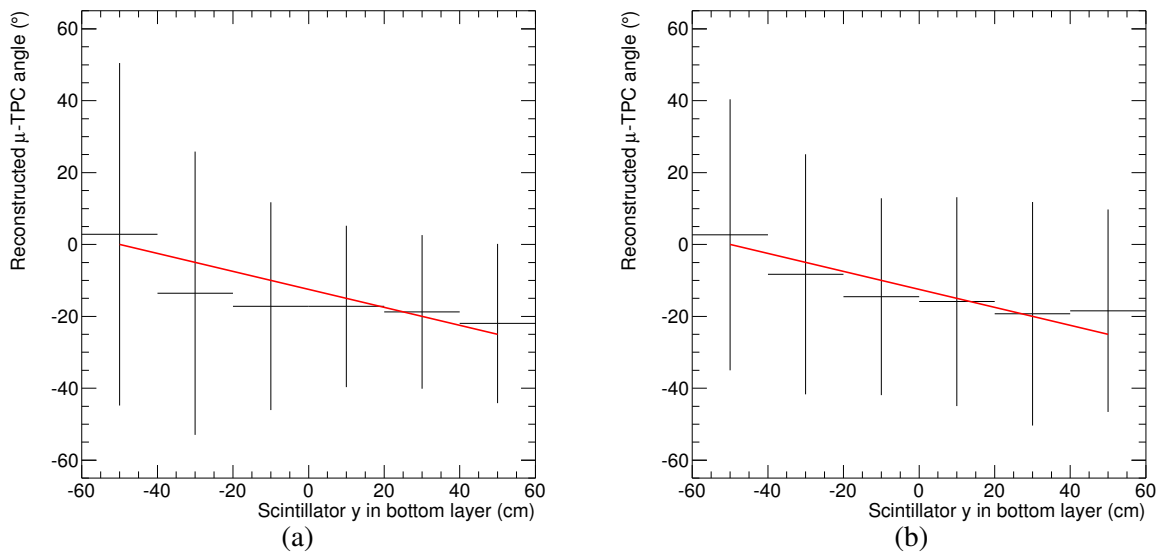


Figure 29: Average track angle of incidence, reconstructed in μ TPC mode, as a function of y -trigger. (a) uses only clusters with at least 3 hits, whereas (b) uses only clusters with exactly 2 hits. The red line indicates the actual track angle as function of y -trigger, ranging from 0° at $y = -50$ cm, to -25° at $y = +50$ cm. The arrival time of each strip has been corrected for time slewing. The FD cut is applied.

6.3 Effect of the RMS TDO noise

We have measured the RMS noise of the TDO digitized value to be $\simeq 3$ mV which corresponds to 5 ns when using a 1000 ns TAC scale⁷. We use a toy Monte Carlo to evaluate the angular resolution due to this noise in the ideal case that the micromega behaves as a TPC. In the ideal case, the arrival time

⁷ The study in Ref. [11] uses a 500 ns TAC scale and therefore the RMS noise in ns is halved.

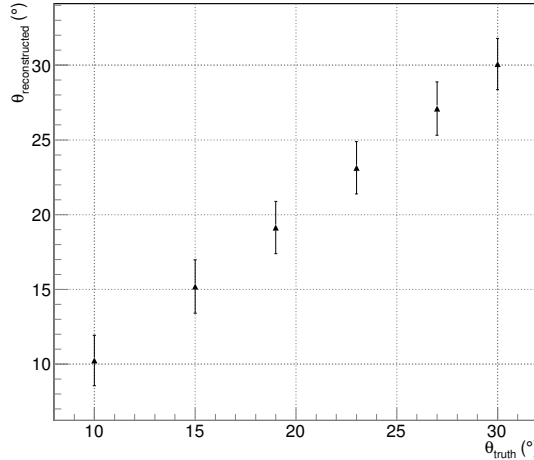


Figure 30: Average track angle of incidence, θ , reconstructed in μ TPC mode as a function of the real angle in simulated events (see text) for tracks with 10, 15, 19, 23, 27, and 30° angles.

of a strip signal corresponds to the distance between the ionization-energy deposit in the drift gap and the micromega mesh. We generate tracks with six different angles of 10, 15, 19, 23, 27, and 30° (the ionization charge is collected by 2, 3, 4, 5, 6, and 7 strips, respectively). The drift velocity is set to 20 ns/1 mm, and the arrival time on each strip is smeared with a Gaussian function with a 5 ns RMS.

We reconstruct the track’s direction as in the data. The average reconstructed angle as a function of the real angle is shown in Fig. 30. The angular resolution due to the TDO RMS noise is approximately 2°, and negligible with respect to the $\approx 30^\circ$ resolution measured in the data.

6.4 Angular accuracy of the μ TPC analysis and geometrical cutoffs

Figures 31 and 32 show the distributions of $\tan \alpha$, the reconstructed track slopes for events triggered by different bottom layer scintillators (the track angle θ increases from 0 to 25° in 5° steps with a 1.5° RMS spread). Distributions for track angles below 10° are shown for completeness. For track angles above 10°, the μ TPC mode determines with a 100 μ m accuracy the x position of an incident particle if its angle of incidence can be reconstructed with a 2° accuracy. One observes that: (a) the average value of the fitted slope ($\tan \alpha$) is loosely correlated with the track’s angle of incidence; (b) the RMS deviation of the $\tan \alpha$ distributions decreases with increasing track angle because the number of degrees of freedom of the fits (or number of fitted strips) increases but is substantially much larger than what needed⁸.

Figures 33 and 34 show the distributions of the reconstructed angle θ . There is a geometrical cutoff to the absolute value of angles θ reconstructed with 2-strip clusters due to the maximum drift length (5 mm) and the strip pitch (0.4 mm). The cutoff $\theta_{\min} = \tan^{-1}(0.4\text{mm}/5\text{mm}) = 5^\circ$ is clearly visible in Fig. 33.

For ≥ 3 strips clusters, θ_{\min} increases with the number of strips in a cluster which in turn increases with the track’s angle. The minimum angle increases from $\theta_{\min} = 10^\circ$ for 3-strip clusters to 22° for 5-strip clusters. This angular cutoff sculpts the distributions in Fig. 34. Together with the shrinking of the RMS of the $\tan \alpha$ distributions with increasing track angle, it gives the false impression of a good angular resolution.

⁸ The reader should compare RMS deviations in Fig. 31 (2 strips) to Fig. 32 (≥ 3 strips) and keep in mind that the number of cluster strips in Fig. 32 increases with the track angle (see Fig. 26). In Fig. 31, the number of degrees of freedom of the fit does not increase, as the figure is restricted to clusters with exactly 2 hits. However, for large angle tracks the 2-hit clusters are more likely to contain holes, increasing the distance between strips in the cluster and thus restricting possible angles for the fit.

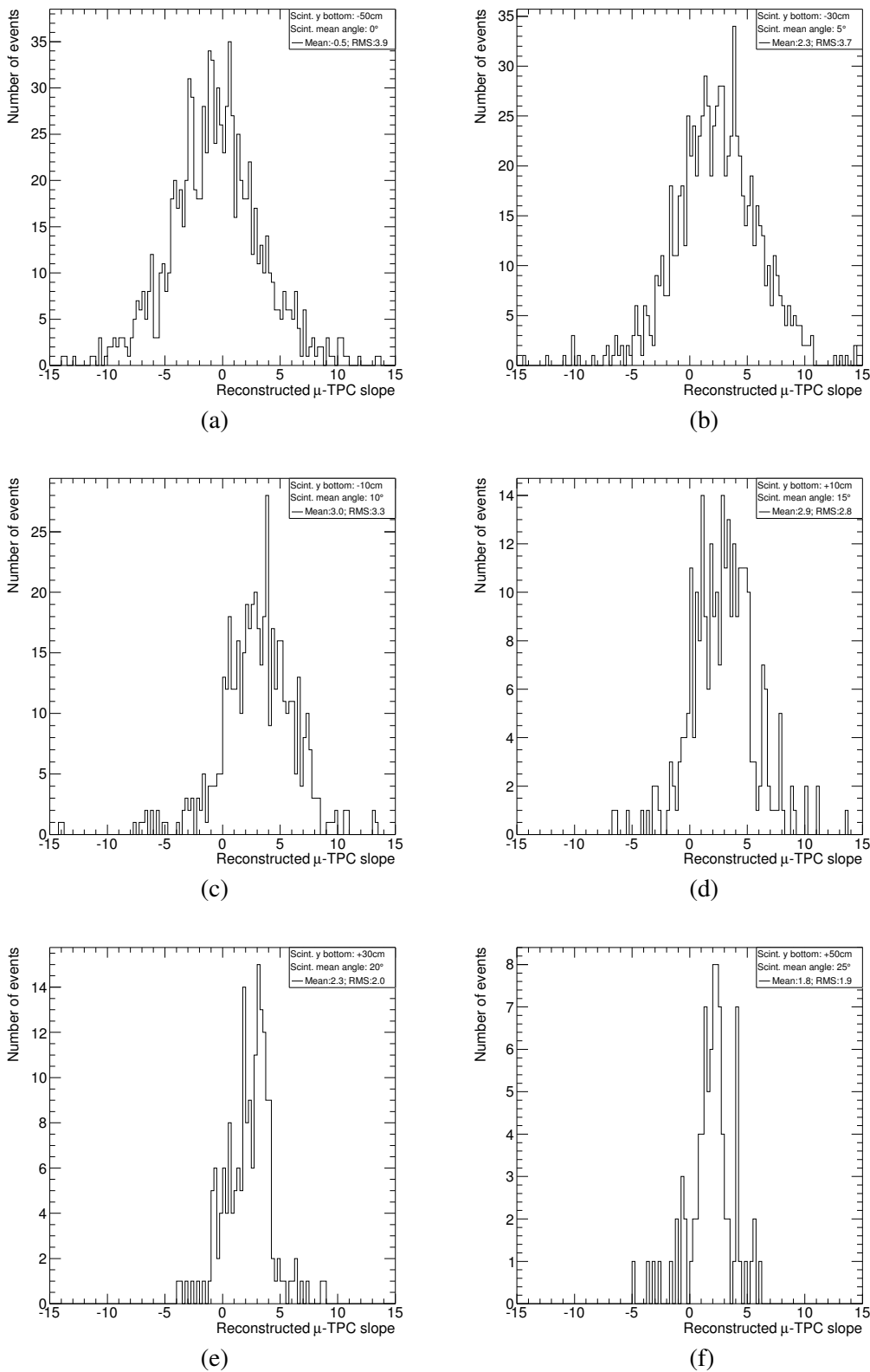


Figure 31: Distributions of $\tan \alpha$ for events triggered by different bottom scintillators, using clusters with exactly two strips. Average track angles are (a) 0° , (b) 5° , (c) 10° , (d) 15° , (e) 20° and (f) 25° .

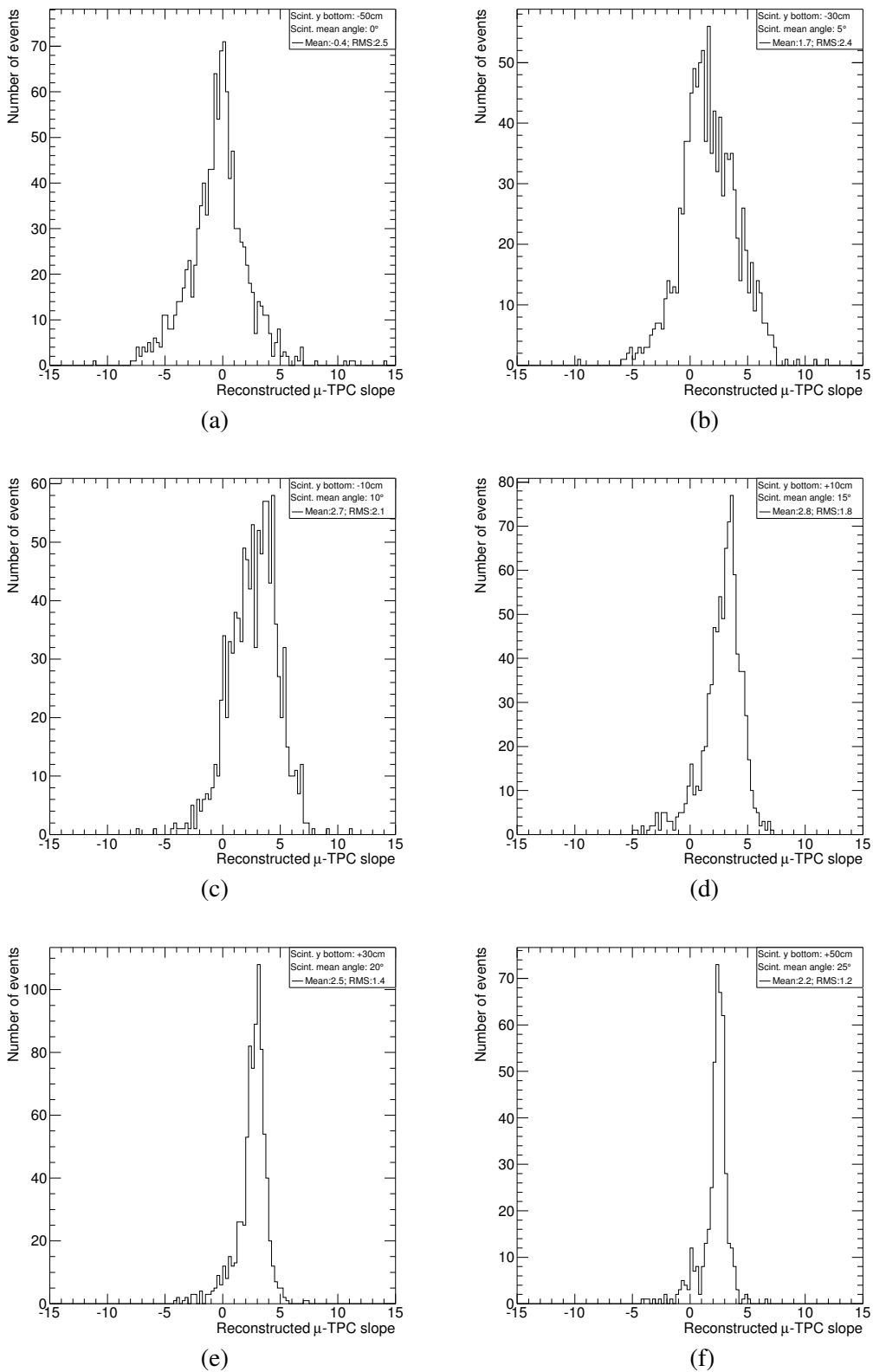


Figure 32: Distributions of $\tan \alpha$ for events triggered by different bottom scintillators, using clusters with at least three strips. Average track angles are (a) 0° , (b) 5° , (c) 10° , (d) 15° , (e) 20° and (f) 25° .

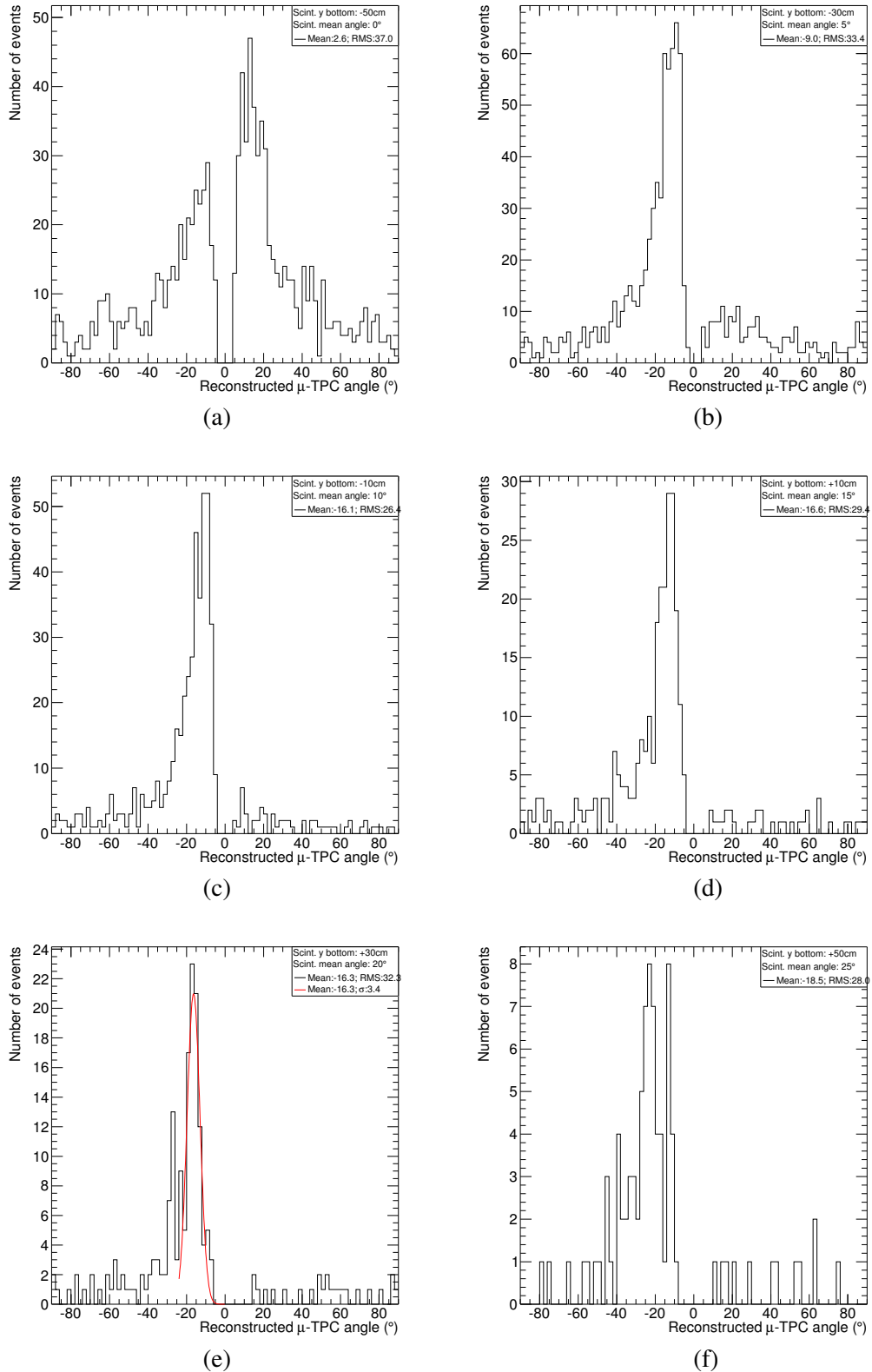


Figure 33: Distributions of the track angle θ reconstructed with 2-strip clusters for events triggered by different bottom scintillators. Track angles correspond to (a) 0° , (b) 5° , (c) 10° , (d) 15° , (e) 20° and (f) 25° . The red line is a fit to the θ distribution similar to that in Ref. [11].

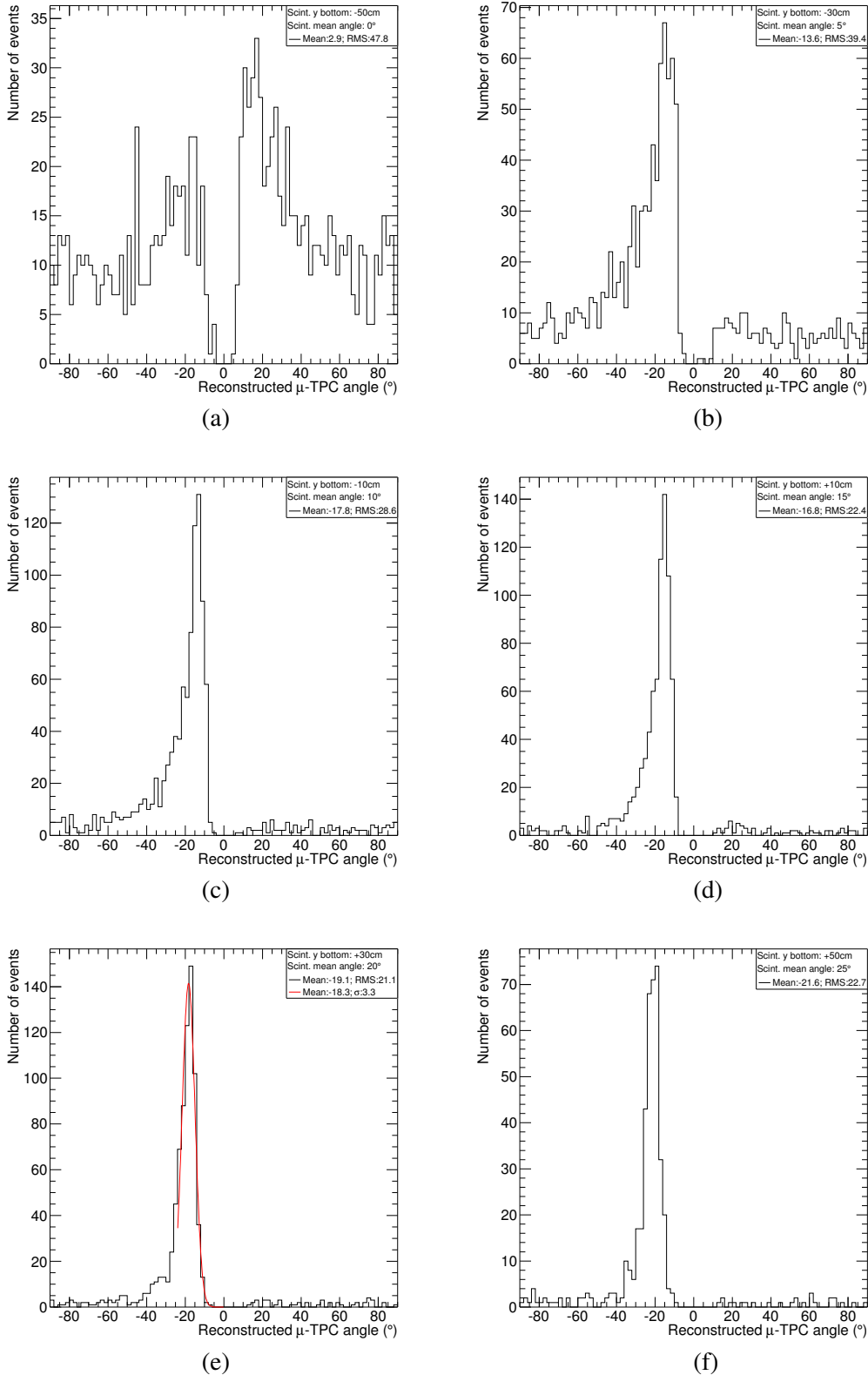


Figure 34: Distributions of the track angle θ reconstructed with ≥ 3 -strip clusters for events triggered by different bottom scintillators. Track angles correspond to (a) 0° , (b) 5° , (c) 10° , (d) 15° , (e) 20° , and (f) 25° . The red line is a fit to the θ distribution similar to that in Ref. [11].

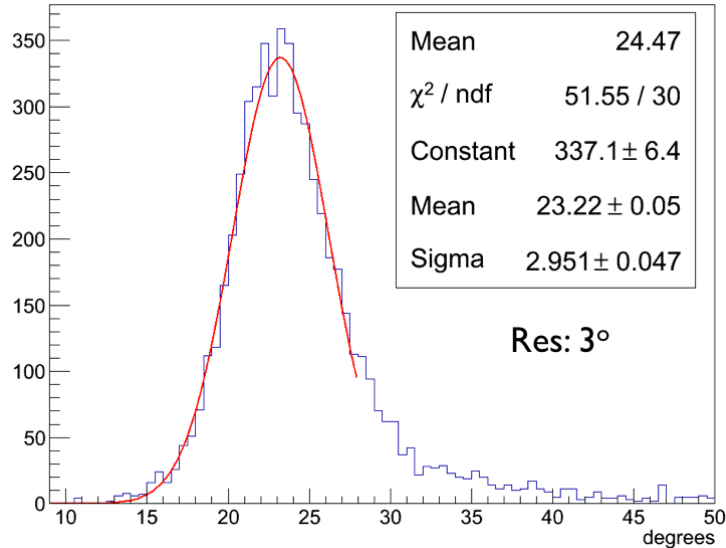


Figure 35: Angular distribution of tracks at 20° . This figure is reproduced from Ref. [11].

To make the point more precisely, we compare the θ distribution in Fig. 34 (e) (corresponding to 20° tracks) with that in Fig. 35, reproduced from Ref. [11] (our negative angles correspond to positive angles in the latter plot). One notes that the distributions are very similar but the latter does not show reconstructed angles below θ_{\min} . A fit similar to that performed in Ref. [11] (i.e. the small angular region below θ_{\min} indicated by the red fit line) with a Gaussian function yields an average reconstructed angle of 18° and RMS of 3.3° consistent with the finding in [11]. However, approximately 20% of events lie outside the $\pm 3\sigma$ range of the fit, and the RMS deviation of the reconstructed-angle distribution is actually 21° .

6.5 Reconstructed clusters with and without holes

As shown by Fig. 14 (b), approximately 10% of the reconstructed clusters contain holes. In Fig. 36 we compare the averages and the RMS deviations of the reconstructed track angle distribution using clusters with and without holes. Reconstructed angular distributions are not appreciably affected by the presence of holes. However, because the RMS deviation of the reconstructed-angle distributions decreases with increasing distance between the first and last strip in a cluster, ironically 2-strip clusters with holes provide the smallest RMS deviation.

6.6 On the large uncertainty in determining the x position of large angle tracks

In this subsection we show that this large uncertainty is produced by the characteristics of the VMM1 chip. The first problem is that the VMM1 threshold has to be set too high to compensate for the unevenness of different channels without losing any of them. Figure 37 compares the multiplicity distribution of clusters produced by tracks with 0° and 25° angles of incidence. The ionization charge Q produced by 0° tracks is on average collected by 2 strips. The same ionization charge produced by 25° tracks is collected by 6 strips. Because each strip collects a charge $Q/6$ instead of $Q/2$, strips' signals are frequently below threshold, and the average multiplicity is four with a significant tail down to multiplicity one.

In those cases in which only one strip is detected, the x -resolution is $6 \text{ strips} \cdot 0.4 \text{ mm(pitch)} / \sqrt{12} = 0.7 \text{ mm}$. In those cases where two strips are detected, the track's angle reconstructed with a 30° uncertainty yields a x_{clu} uncertainty of 1.8 mm . When 3 or more strips are detected, the track's angle reconstructed with a 20° uncertainty yields a x uncertainty of 1.1 mm . These uncertainties are more than

Not reviewed, for internal circulation only

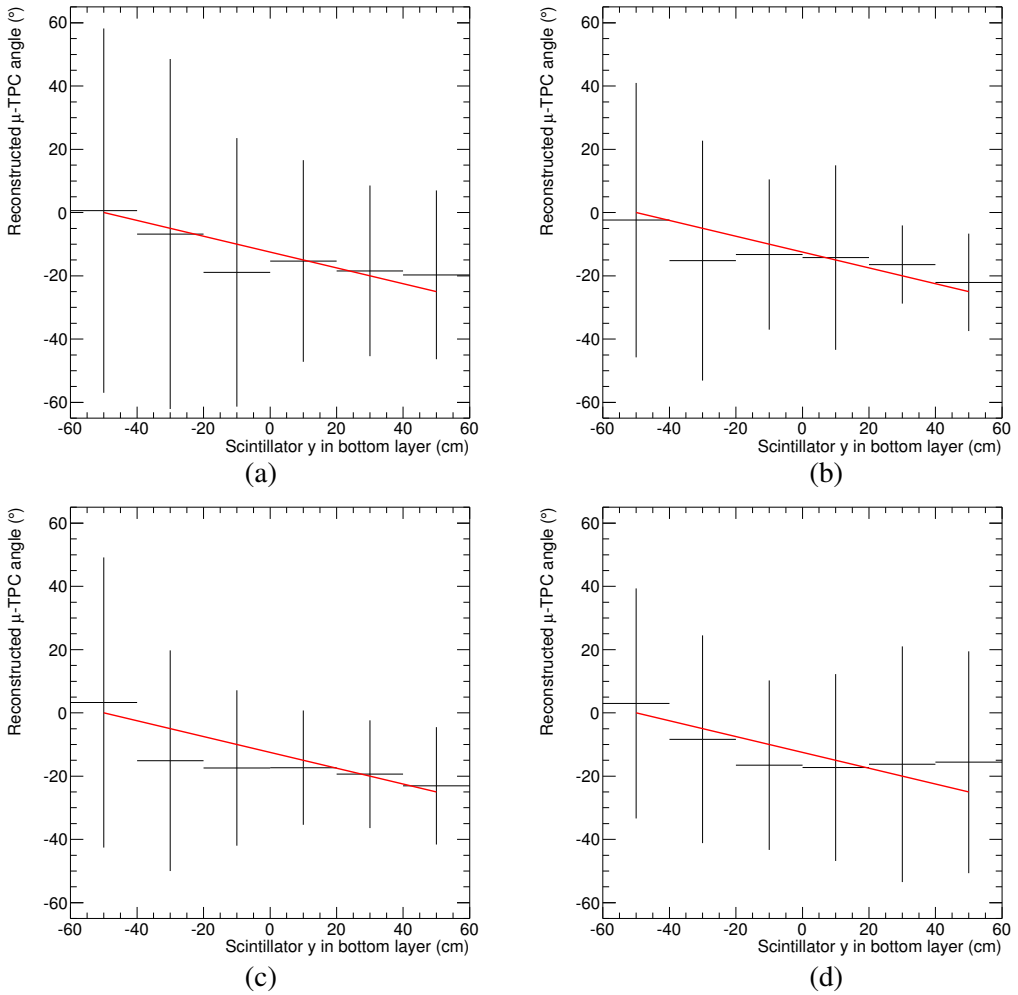


Figure 36: Distributions of reconstructed track angle θ for events triggered by different bottom scintillators. Plots (a) and (c) are for ≥ 3 -strip clusters with and without holes, respectively. Plots (b) and (d) are for 2-strip clusters with and without holes, respectively. The FD cut is applied.

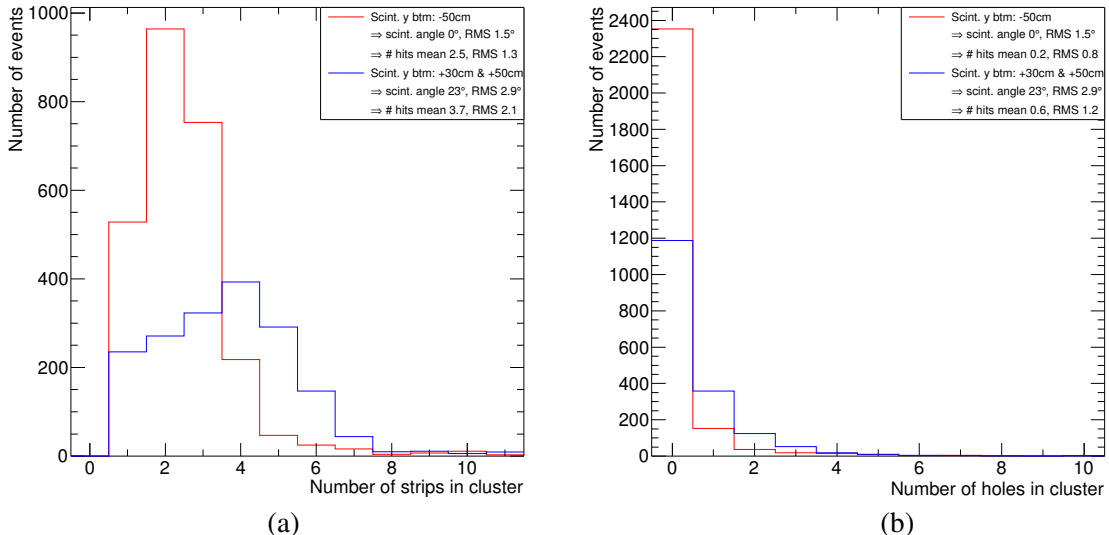


Figure 37: Comparisons of (a) hit multiplicity and (b) number of holes distributions for clusters produced by tracks with 0° and $23^{\circ} \pm 1.9$ angles of incidence. The FD cut is applied.

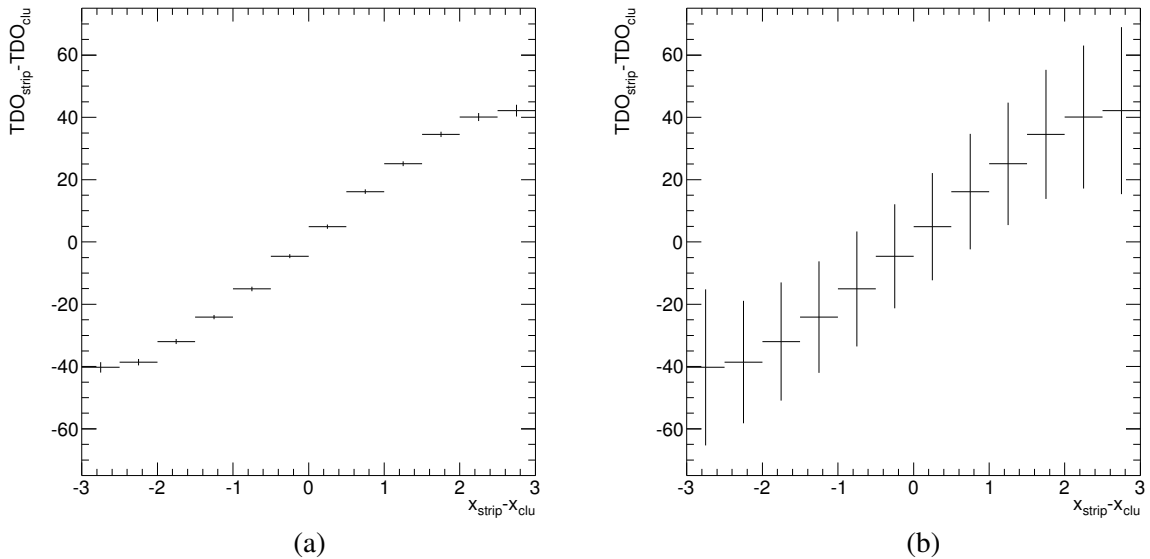


Figure 38: Average of $\text{TDO}_{\text{strip}} - \text{TDO}_{\text{clu}}$ as a function of $x_{\text{strip}} - x_{\text{clu}}$ (see text) for tracks at 23° angles with a RMS spread of 2.9° . The errors on the left plot represent the uncertainties of the averages and those on the right plot the RMS deviations. The FD cut is applied.

an order of magnitude larger than those anticipated in the NSW TDR [5, Sec.2].

With a mesh voltage of 550 V, we operate the micromega very close to the breakdown voltage. At this voltage, the distribution of the charge of each strip integrated by the VMM1 chips spans from the threshold (a few fC) up to saturation (120 fC). Using VMM1 gains larger than 9 mV/fC or operating the micromega at breakdown voltage will rescue some signals below threshold but will saturate a large fraction of the charge distribution creating new problems⁹.

The second problem is the accuracy of the VMM1 peaktime detector in determining the arrival time of the drift electrons that fire a given strip. We measure it using data. We use events triggered by the last two bottom scintillators, thus selecting tracks at 23° angles with a RMS spread of 2.9° . We use ≥ 3 -strip clusters. For each cluster we evaluate the x position of the cluster in number of strips, x_{clu} , and the average TDO of the cluster, TDO_{clu} ¹⁰. We then plot the difference between the TDO of a strip in a cluster, $\text{TDO}_{\text{strip}}$ and TDO_{clu} versus the difference of the strip number, x_{strip} , and x_{clu} for all events. The averages and RMS deviations of these distributions are shown in Fig. 38. One sees that, averaged over many events, tracks with a 23° angle deposit charge over six strips, as expected, though only a few of these strips produce a signal on an event-by-event basis.

The VMM1 measures the time at which, at the end of the drift time, a peak is found after integrating for 100 ns the charge induced by the ion collection and by the electron charge diffusing along the resistive strips. The time difference between the first and last strip in a cluster is on average consistent with the expected drift time difference of about 100 ns. There are appreciable non-linearities that could be corrected for, but on average the peaktime is a measure of the drift arrival-time.

The data also show that the RMS deviation between the drift arrival-time and the VMM1 peaktime on an event-by-event basis is approximately 20 ns. This method underestimates the RMS deviation. When measuring the PDO fluctuation of a strip with respect to the measured average, the RMS deviation

⁹In order to reconstruct the x position of a 25° track with a $100 \mu\text{m}$ accuracy using the μTPC mode one needs an angular resolution of 2° which in turn requires a 5 ns RMS resolution in determining the drift time from the strip signal. As shown by Fig. 29, slewing time corrections are larger than 5 ns and cannot be determined if most of the charge distribution is saturated.

¹⁰We calculate x_{clu} as the PDO-weighted average of the strip number. For TDO_{clu} , the average is not charge weighted.

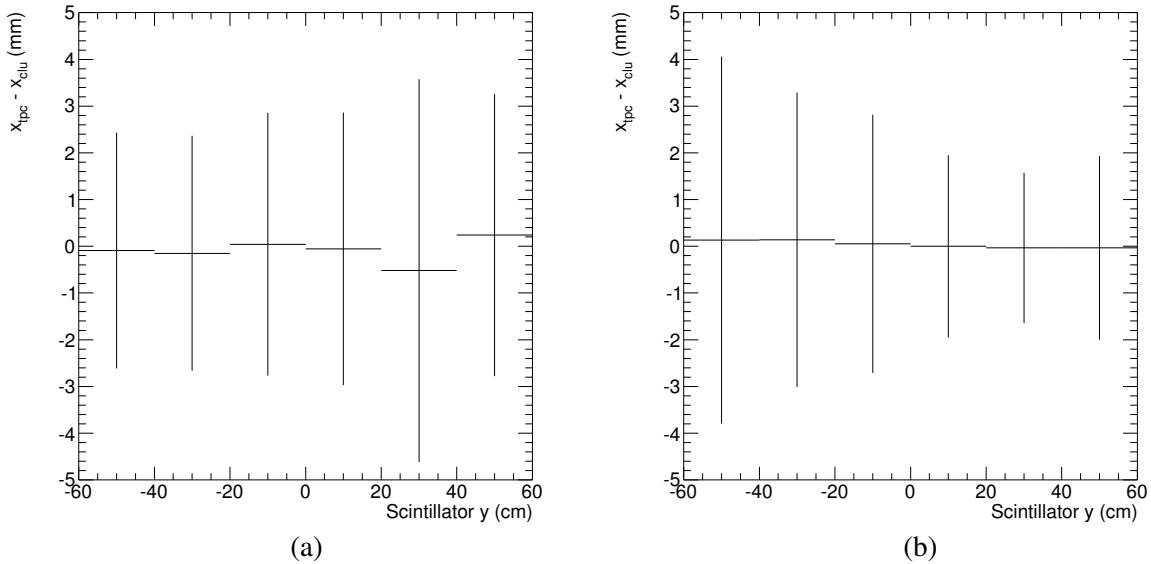


Figure 39: Average and RMS deviation of $x_{\text{TPC}} - x_{\text{clu}}$ (see text) distributions as a function of y -trigger for (a) 2-strip clusters and (b) ≥ 3 -strip clusters. The FD cut is applied.

grows to 25 ns¹¹. As mentioned earlier, in order to reconstruct the x position of a 25° track with a 100 μm accuracy using the μ TPC mode one needs an angular resolution of 2° which in turn requires a 5 ns accuracy in determining the drift arrival-time using a strip signal. Inserting a 25 ns resolution, our toy Monte Carlo (see Section 6.3) yields an RMS angular resolution of approximately 30°, in the ball park of the angular resolutions measured in the data.

6.7 Measurement of the x position resolution using charge barycenter and μ TPC modes

In the charge-barycenter mode, the x position of a track is derived as $x_{\text{clu}} = \sum q_i x_i / \sum q_i$ (mm), where q_i is the charge collected by the strip at x_i . If $z_d = 5$ mm is the drift thickness, x_{clu} measures the x position of a track at $z_d/2 = 2.5$ (mm).

In the μ TPC mode, the PDO time (ns) of each strip i is converted into a coordinate $z_i = A - PDO_i/B$, where PDO_i is the peaktime (ns) of strip i , $B=20$ ns/mm is the inverse of the drift velocity, and A is an arbitrary constant. The (x_i, z_i) points in a cluster are fitted with a straight line $z = mx + c$, and the cluster x position is evaluated as $x_{\text{TPC}} = (2.5 - c)/m$ (mm). The constant A is then tuned to yield $\langle x_{\text{clu}} - x_{\text{TPC}} \rangle = 0$.

Figure 39 shows the average and RMS of $x_{\text{TPC}} - x_{\text{clu}}$ distributions as a function of y trigger (track angles from 0° to 25° , in 6 steps of 5° with a 1.5° RMS deviation). The same difference is shown in Fig. 40 as a function of the cluster multiplicity for tracks with $\geq 20^\circ$ angles of incidence. The RMS deviation for angles of incidence larger than 10° is $\simeq 2$ mm. As shown in the previous section, for tracks with angles larger than 10° the x_{clu} uncertainty cannot be larger than 0.7 mm. It follows that the uncertainty of x_{TPC} is in the ballpark of 2 mm. This direct evidence is consistent with the earlier measurement of the angular resolution.

In the following, we further investigate the x resolution by exploiting the good angular resolution of the HCRT telescope. Each bottom scintillator selects tracks with angle $\theta \pm 2.5^\circ$ in six steps of 5° with RMS angle-uncertainty of 1.5° . For tracks triggered by a given scintillator, we fit x_{clu} in μTPC mode, referred to as x_{true} , constraining the parameter m to $\tan(\theta + 90^\circ)$. To evaluate the uncertainty due to the

¹¹This RMS difference between the drift arrival-time and the VMM1 peaktime for a single strip is consistent with the overall width of the time distribution of the ART-emulated signal shown in Fig. 21.

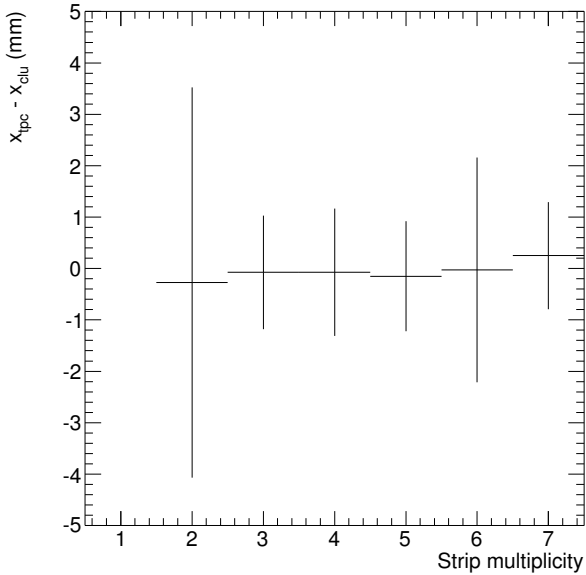


Figure 40: Average and RMS deviation of $x_{\text{TPC}} - x_{\text{clu}}$ (see text) distributions as a function of the cluster multiplicity for tracks with angle of incidence $\geq 20^\circ$. The FD cut is applied.

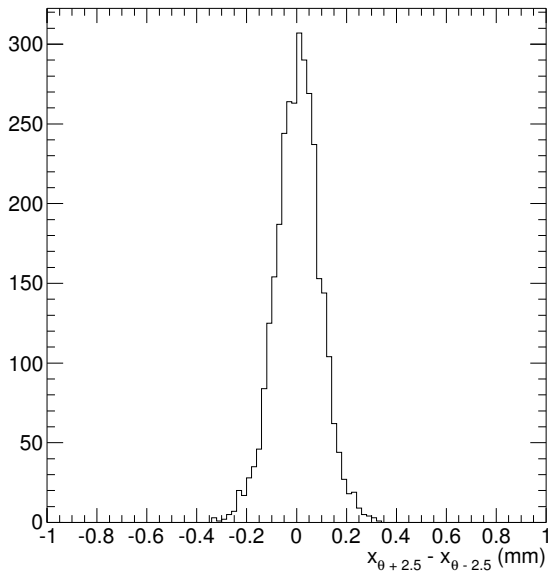


Figure 41: Distribution of the difference between x_{true} values calculated at $\tan(\theta + 90 + 2.5^\circ)$ and $\tan(\theta + 90 - 2.5^\circ)$ for tracks with angle $\theta \geq 10^\circ$.

angular acceptance of a given y -trigger, we also fit the data constraining m to $\tan(\theta + 90 \pm 2.5^\circ)$. Figure 41 shows the distribution of the difference of the x_{true} values obtained by setting m equal to $\tan(\theta + 90 + 2.5^\circ)$ and $\tan(\theta + 90 - 2.5^\circ)$. The RMS deviation is 0.1 mm from the full angular spread of $\pm 2.5^\circ$, corresponding to less than 0.05 mm for an RMS angular spread of $\pm 1.5^\circ$.

Figure 42 shows the average and RMS deviation of $x_{\text{clu}} - x_{\text{true}}$ as a function of y -trigger. We note that 2-strip clusters corresponding to 0° tracks' angles of incidence yield a RMS deviation better than 0.1 mm (at least, it proves that our measurements have this kind of accuracy). As expected, the resolution deteriorates up to 0.8 mm for 2-strip clusters produced by 25° tracks. For ≥ 3 -strip clusters, the resolution

Not reviewed, for internal circulation only

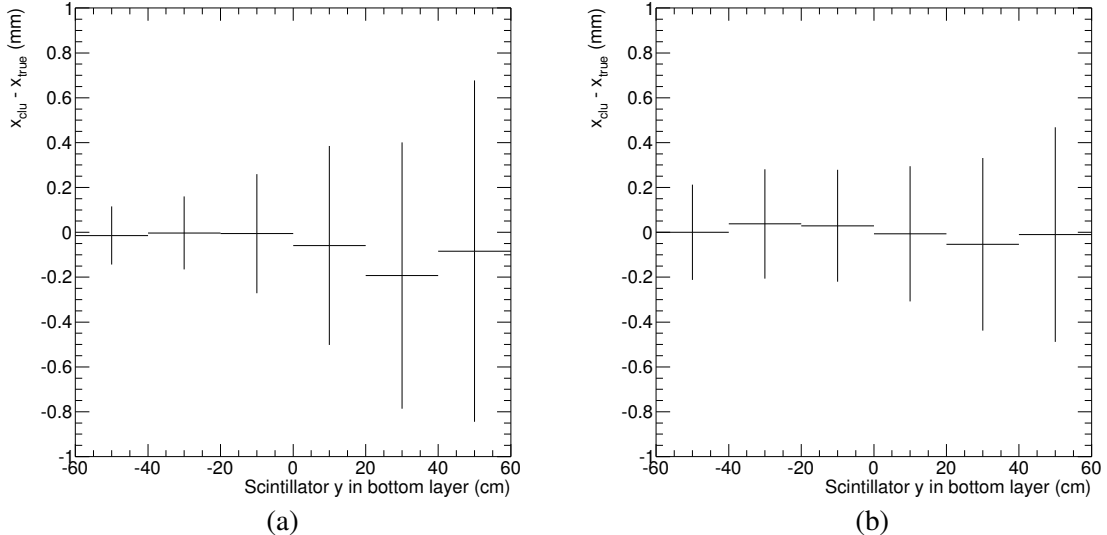


Figure 42: Average and RMS deviation of $x_{\text{clu}} - x_{\text{true}}$ (see text) distributions as a function of y -trigger for (a) 2-strip clusters and (b) ≥ 3 -strip clusters. The FD cut is applied.

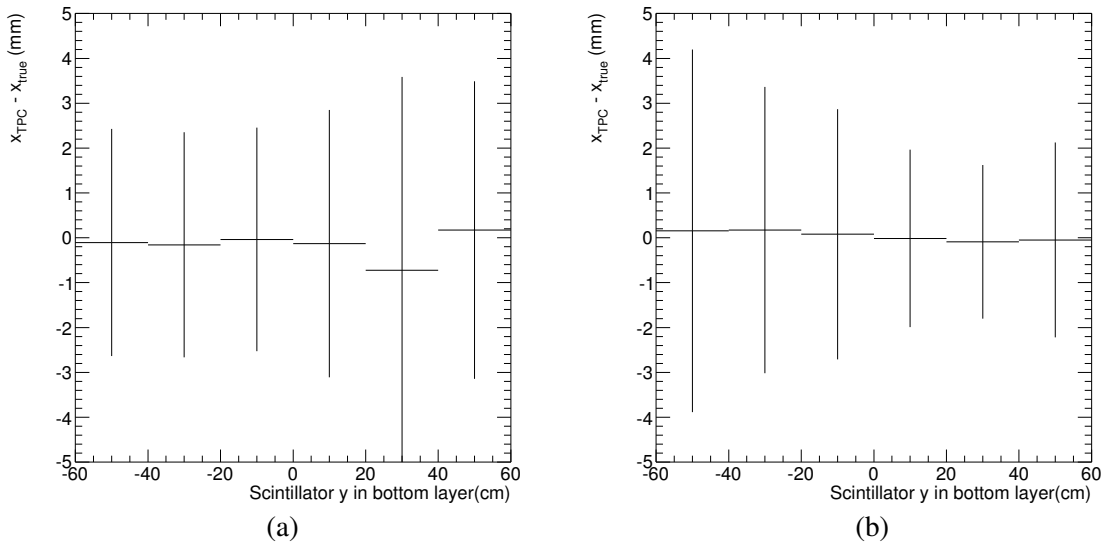


Figure 43: Average and RMS deviation of $x_{\text{TPC}} - x_{\text{true}}$ (see text) distributions as a function of y -trigger for (a) 2-strip clusters and (b) ≥ 3 -strip clusters. The FD cut is applied.

is 0.2 mm at 0° and worsens to 0.5 mm for tracks with 25° angles.

Figure 43 shows analogous plots for $x_{\text{TPC}} - x_{\text{true}}$. The obvious conclusion is that the μ TPC mode applied to micromega detectors instrumented with VMM1 readout yields a x -position accuracy an order of magnitude worse than that required by the NSW TDR [5].

6.8 Accuracy of the x -position measurement using the charge barycenter

The fact that the RMS deviation of $x_{\text{clu}} - x_{\text{true}}$ in Fig. 42 can be as large as 0.5 mm does not mean that the resolution of x_{clu} is that bad. In fact, having fixed the angle θ in the μ TPC fits, x_{true} is still affected by the time accuracy of the cluster-TDO. We prove this with a toy Monte Carlo, in which the number of strips collecting charge is the drift thickness (5 mm) divided by $\tan \theta$ times the strip pitch (0.4 mm). We define x_{gen} as the x -position of the track at $z = 2.5$ mm. The number of cluster strips with a signal is generated

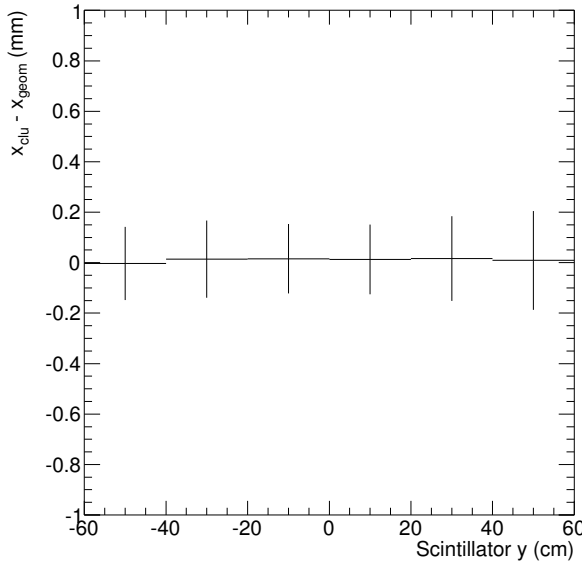


Figure 44: Average and RMS deviation of the difference between x_{clu} values calculated with and without charge weighting as a function of y -trigger. The FD cut is applied.

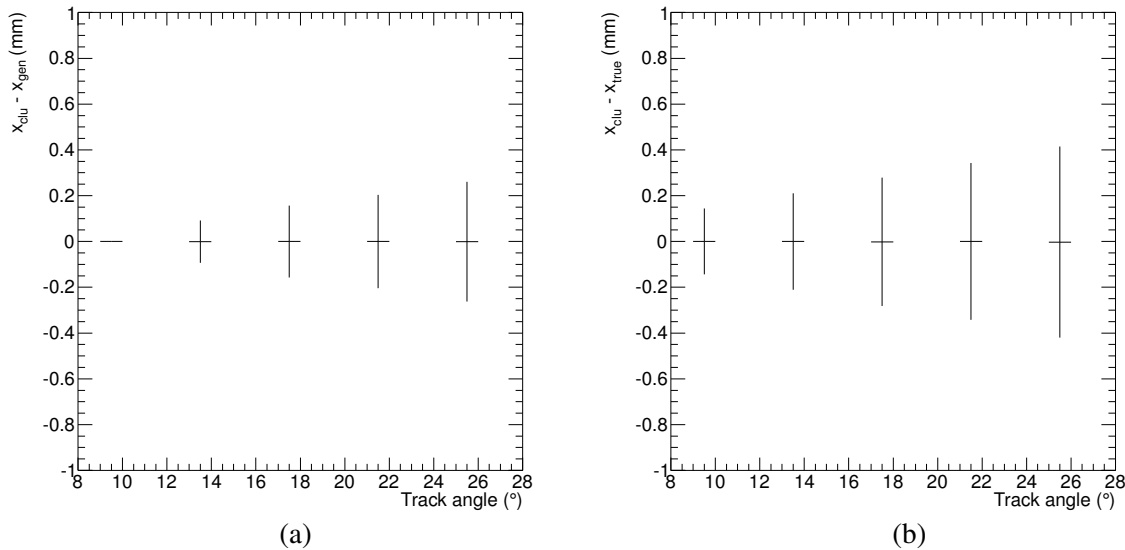


Figure 45: Average and RMS deviation of the simulated (a) $x_{\text{clu}} - x_{\text{gen}}$ and (b) $x_{\text{clu}} - x_{\text{true}}$ distributions for different track angles.

from the multiplicity distribution in the data for tracks with that angle. We then require that the number of strips with a signal is at least 2, to enable comparison with μ TPC performance. The drift time of each fired strip is then smeared with a Gaussian function with a 25 ns RMS deviation as measured in the data. The cluster barycenter is calculated as the average of the strip x -position. As shown with cosmic muon data in Fig. 44, this method yields a result consistent with the charge-weighted barycenter.

Figure 45 shows the average and RMS resolution of simulated $x_{\text{clu}} - x_{\text{gen}}$ and $x_{\text{clu}} - x_{\text{true}}$ distributions. Figure 46 shows the average and RMS resolution of simulated $x_{\text{TPC}} - x_{\text{gen}}$ and $x_{\text{TPC}} - x_{\text{true}}$ distributions. The simulated $x_{\text{clu}} - x_{\text{true}}$ and $x_{\text{TPC}} - x_{\text{true}}$ distributions are in fair agreement with the data. Therefore, it seems fair to conclude that the charge-barycenter provides better accuracy than the μ TPC mode at all track angles. The x -resolution of the barycenter mode, $\simeq 200 \mu\text{m}$ for tracks with a 25° angle, seems to be

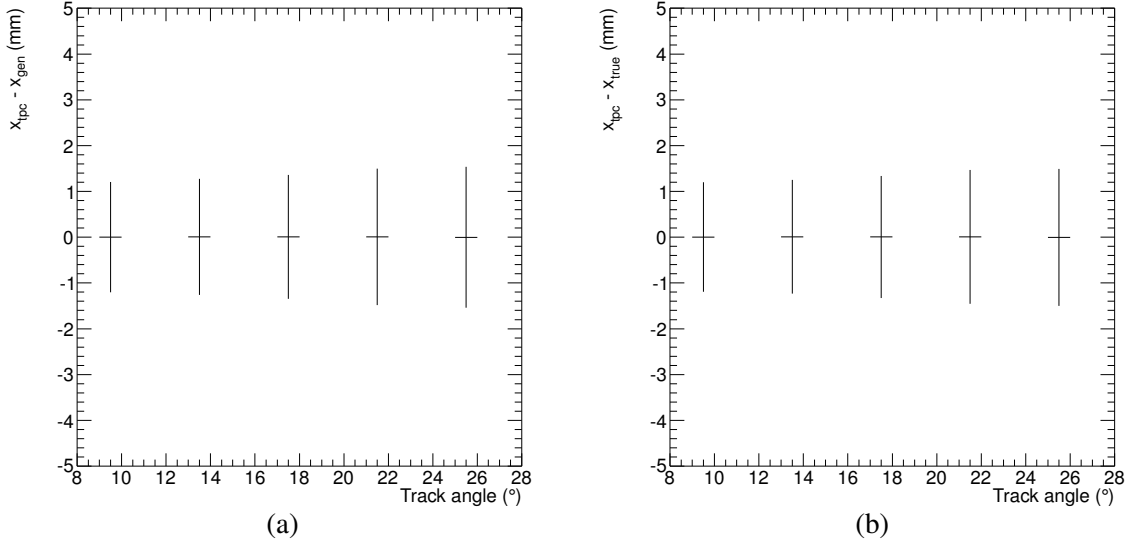


Figure 46: Average and RMS deviation of the simulated (a) $x_{\text{TPC}} - x_{\text{gen}}$ and (b) $x_{\text{TPC}} - x_{\text{true}}$ distributions for different track angles.

a factor of two better than that anticipated in the NSW TDR [5, Fig.5.11]. This accuracy could be further improved if all strips collecting the charge of a large angle track were detected. This may be achieved by providing the possibility to equalize PDO pedestals and VMM thresholds of different channels to within a few millivolts rather than the present few tens of millivolts.

7 Cluster pruning, an attempt to improve the μ TPC resolution

In this section we analyze a high-statistics cosmic-muon run in which we collected 99852 events with hits in the micromega. To maximize the number of strips with a charge larger than the VMM1 threshold we use a mesh voltage of 550 V, a drift voltage of 250 V, and a peaktime of 200 ns. The micromega is positioned in such a way that the bottom scintillators select angles from 0 to 25° in steps of 5° with a RMS deviation of 1.5° . Figure 47 shows the multiplicity distribution for tracks with 0 and $\geq 20^\circ$ angles of incidence. In comparison with Fig. 37, the average multiplicity increases by 10% and the low-multiplicity tail is more suppressed.

Figures 48 and 49, analogous of Figs. 39 and 40, show the average and RMS distributions of $x_{\text{TPC}} - x_{\text{clu}}$ as a function of the track's angle of incidence and the cluster multiplicity, respectively.

Figure 50 shows the distribution of the μ TPC fit residuals for clusters with ≥ 3 strips and tracks with angle of incidence larger than 20° . The study in Ref. [11] removes events in which the μ TPC fit returns large χ^2 values. To avoid introducing unneeded inefficiencies, we prune strips with a residual larger than four if the cluster has at least four strips. We repeat the pruning if there are still residuals larger than four and still at least four surviving strips in the cluster. The result is shown in Fig. 51, and the conclusion is that pruning does not do any harm but does not improve the μ TPC resolution either.

8 Conclusion

We present a detailed study of the performance of a micromega prototype v 3.0 equipped with VMM1 readout. We rediscover a number of known shortcomings, and unfortunately a couple of serious problems which were overlooked when analyzing previous test-beam data. The study shows that a well-run and well-understood cosmic ray telescope is competitive with, if not superior to test beams.

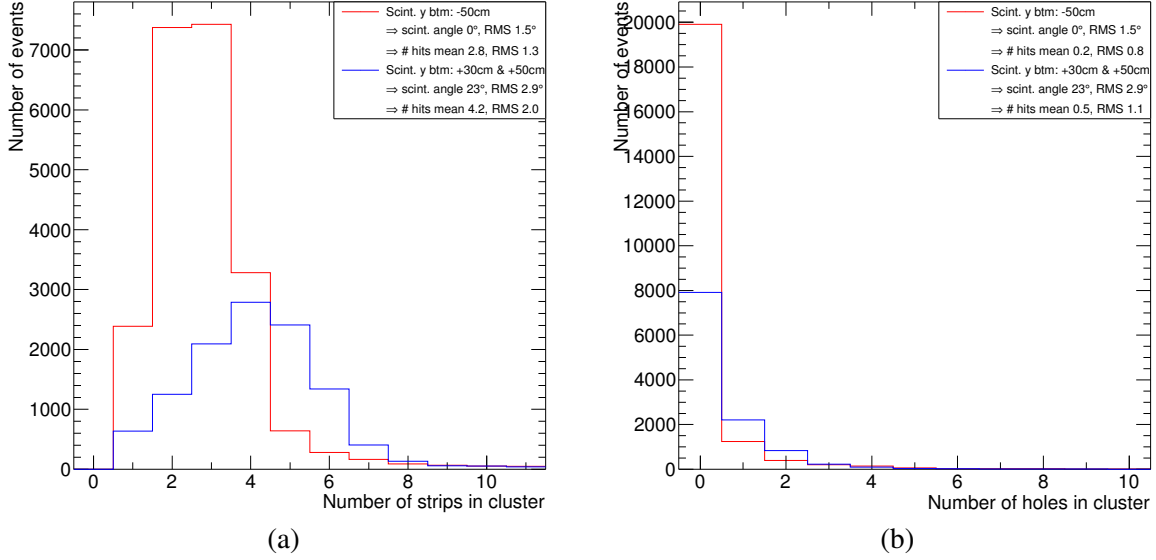


Figure 47: Comparisons of (a) hit multiplicity and (b) number of holes distributions for clusters produced by tracks with 0° and 23° ± 1.9 angles of incidence. The FD cut is applied.

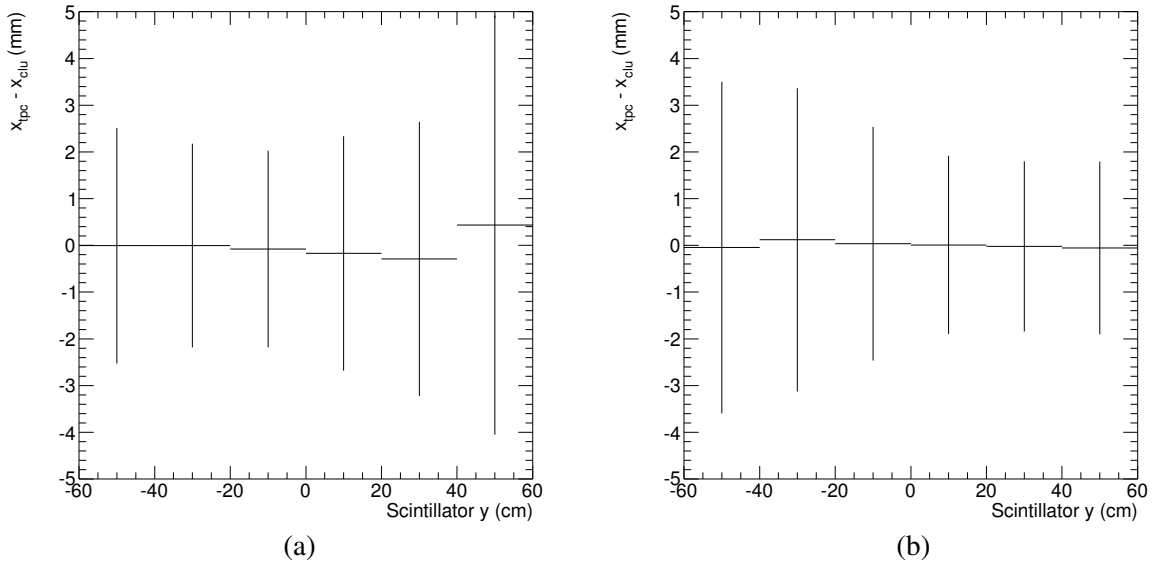


Figure 48: Average and RMS deviation of $x_{\text{TPC}} - x_{\text{clu}}$ (see text) distributions as a function of y -trigger for (a) 2-strip clusters and (b) ≥ 3 -strip clusters. The FD cut is applied.

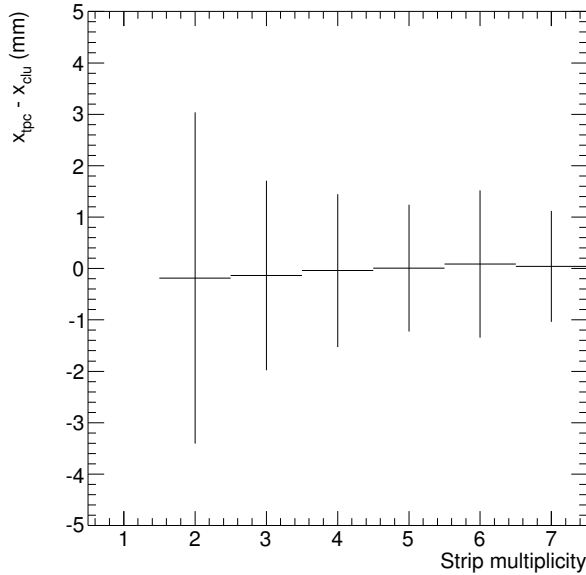


Figure 49: Average and RMS deviation of $x_{\text{TPC}} - x_{\text{clu}}$ (see text) distributions as a function of the cluster multiplicity for tracks with a $\geq 20^\circ$ angle of incidence. The FD cut is applied.

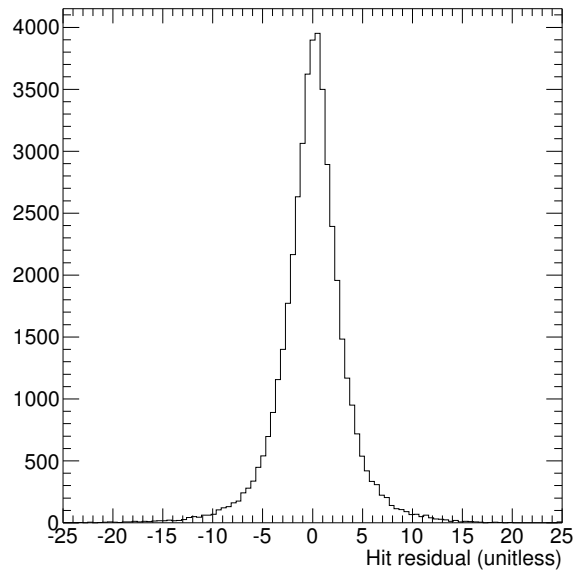


Figure 50: Distributions of the μTPC fit residuals, $(z_{\text{strip}} - z_{\text{fit}})/\sigma$, for clusters with ≥ 3 strips and tracks with angle of incidence larger than 20° . In the fits we use a TDO uncertainty of 5 ns corresponding to 0.25 mm in the z coordinate. The RMS Gaussian deviation of the residuals is 8 ns. The FD cut is applied.

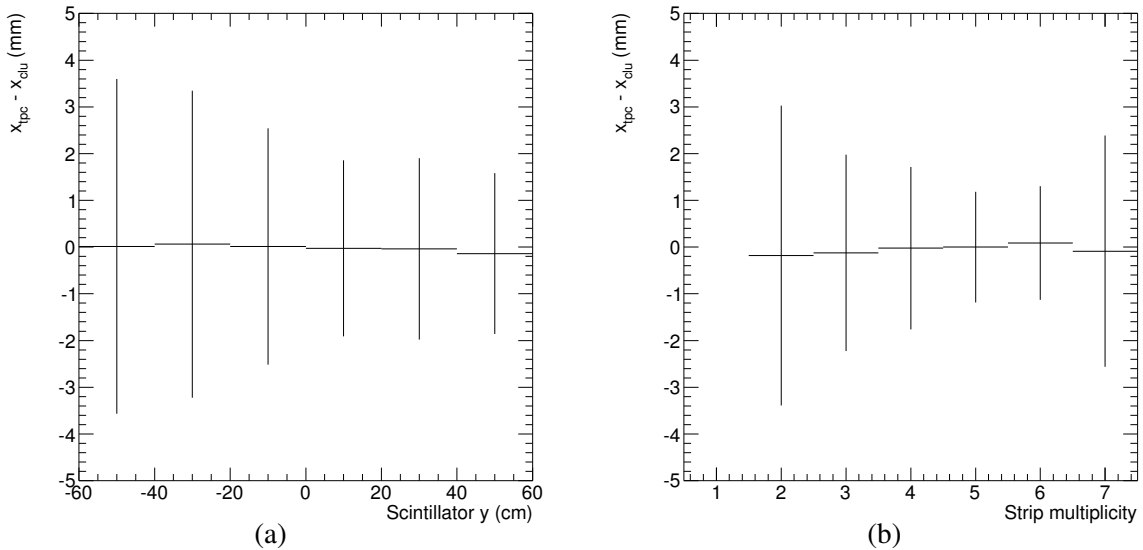


Figure 51: Average and RMS deviation of $x_{\text{TPC}} - x_{\text{clu}}$ (see text) distributions as a function of (a) the track's angle of incidence and (b) the cluster multiplicity for tracks with angle of incidence $\geq 20^\circ$. Hit pruning is applied. The FD cut is also applied.

References

- [1] J. Connors *et al.*, ATL-COM-UPGRADE-2013-019.
- [2] J. Connors *et al.*, ATL-COM-UPGRADE-2013-023.
- [3] J. Connors *et al.*, ATL-COM-UPGRADE-2013-034.
- [4] H. Skottowe, <https://indico.cern.ch/event/316354/contribution/2/material/slides/>;
J. Guimarães da Costa, <http://indico.cern.ch/event/298095/contribution/78/material/slides/>.
- [5] ATLAS New Small Wheel Technical Design Report, ATLAS-TDR-020, CERN-LHCC-2013-006
- [6] R. De Oliveira, private communication: “Usually only DI water with a high pressure spray (100 Bars) is enough. For your detector I’ve been obliged to dip it in a caustic soda bath at 20% concentration at 50° during 5 min followed by a neutralisation bath of $\text{H}_2\text{O} + \text{H}_2\text{O}_2 + \text{H}_2\text{SO}_4$ during 5 min + a high pressure DI water rinse. This treatment removes a thin skin of the Photoimageable coverlay.”
- [7] The QT based data-acquisition software was provided by G. Iakovidis, with our own modifications.
- [8] More VMM1 details can be found at https://twiki.cern.ch/twiki/pub/Atlas/NSWelectronics/VMM1_datasheet_v3a.pdf by G. De Geronimo *et al.*
- [9] V. Polychronakos, *Micromega trigger tests with MSW*, <https://indico.cern.ch/event/298095/session/4/contribution/77/material/slides/1.pdf>.
- [10] T. Alexopoulos, *Highlights from 2013 test-beam analysis*, <https://indico.cern.ch/event/298095/session/4/contribution/60/material/slides/0.pdf>.
- [11] T. Alexopoulos *et al.*, *Performance of the first version of VMM front-end ASIC with resistive micromega detectors*, ATL-UPGRADE-PUB-2014-001

A Appendix: Event displays for μ TPC fit

Figures 52 to 61 show the results of the μ TPC fit for various representative events. When pruning is applied, the results without pruning are denoted in red, while the results with pruning are denoted in black. The horizontal gray dotted line marks 2.5 mm in the z coordinate for reference. The vertical gray dotted line marks the position of the barycenter of the unpruned cluster. The dotted red or black line marks the result of the μ TPC fit with the angle fixed as determined by hits in the bottom scintillator.

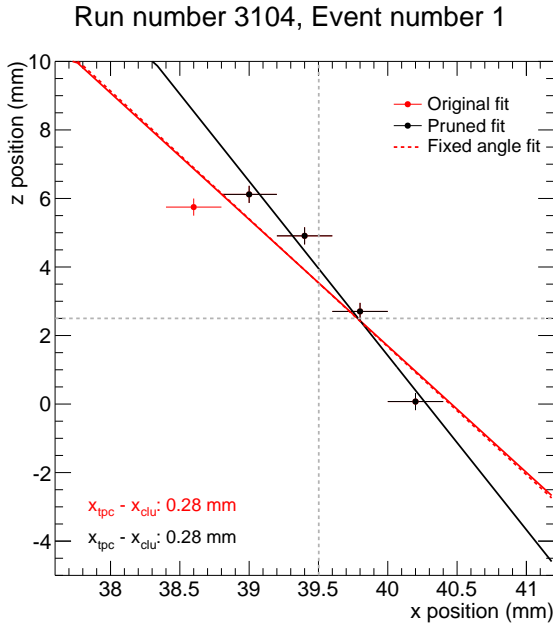


Figure 52: Event display for the first MM event of run 3104. In this case, we can see that the pruning does not bring the result of the μ TPC fit any closer to the measured barycenter. Also, the result of the fixed angle fit matches almost exactly with that of the unconstrained fit for the unpruned cluster.

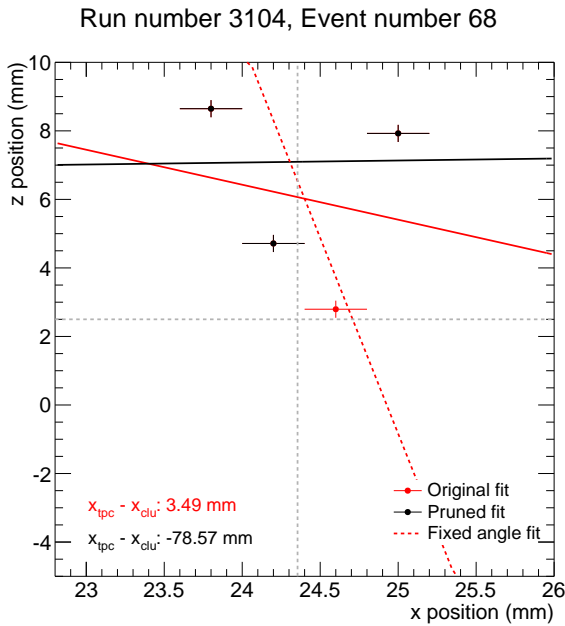


Figure 53: Event display for event 68 of run 3104. In this example, the μ TPC fit with the pruned cluster performs significantly worse than the unpruned cluster.

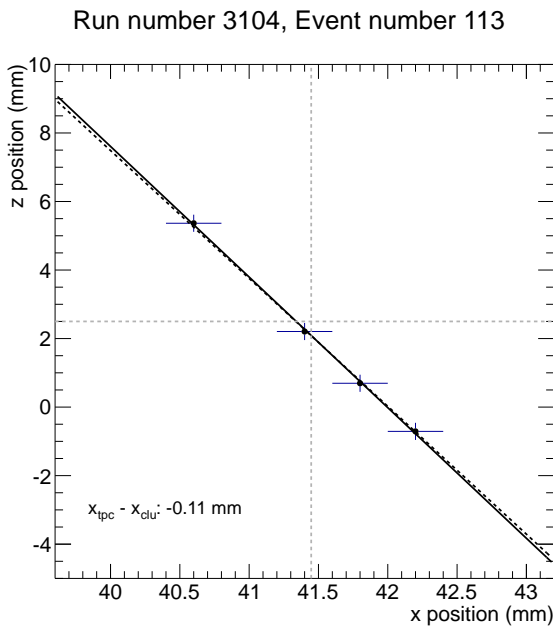


Figure 54: Event display for event 113 of run 3104. In this example, the original fit performs well so there is no pruning needed.

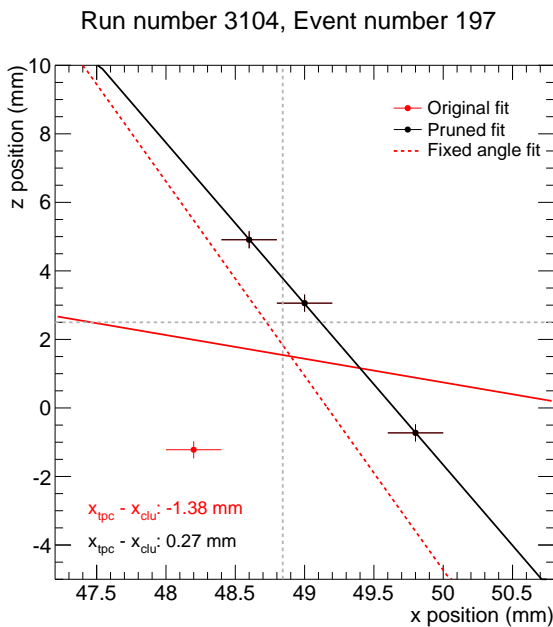


Figure 55: Event display for event 197 of run 3104. In this example, the pruned cluster μ TPC fit does find a center closer to the measured barycenter.

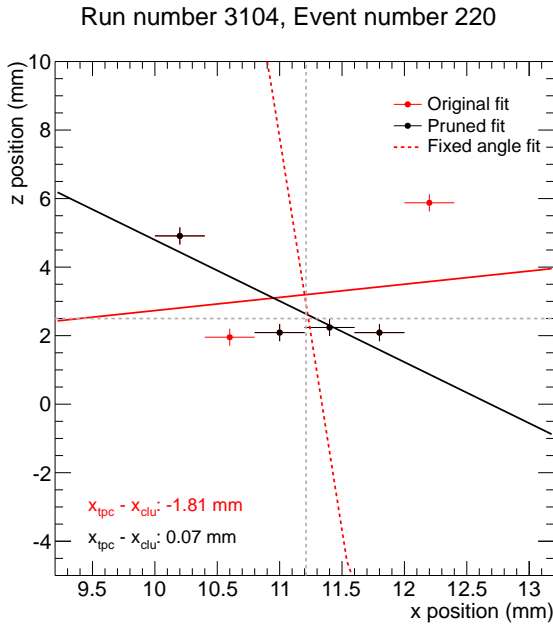


Figure 56: Event display for event 220 of run 3104. In this example, two hits are pruned away and the result is a better μ TPC fit.

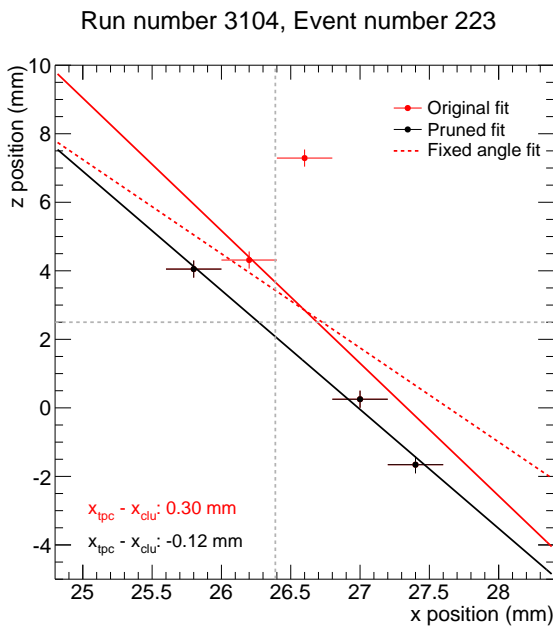


Figure 57: Event display for event 223 of run 3104. In this example, two hits are pruned away, but the absolute distance between the μ TPC center and the barycenter remains nearly the same.

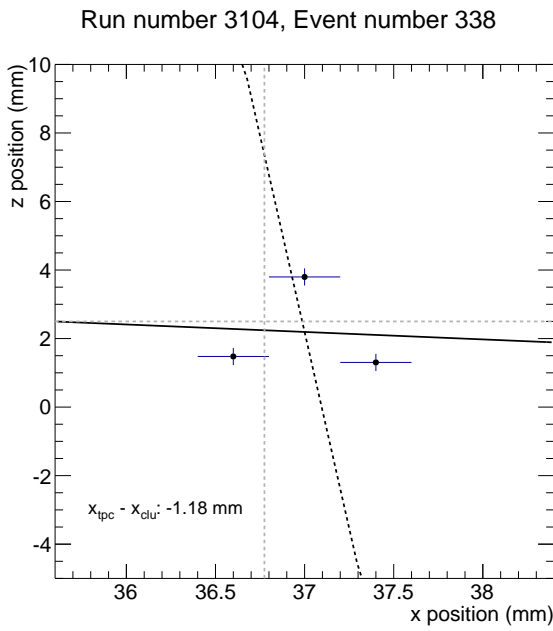


Figure 58: Event display for event 338 of run 3104. This is an example of a bad TPC fit that is not possible to fix via pruning (since there are only 3 hits).

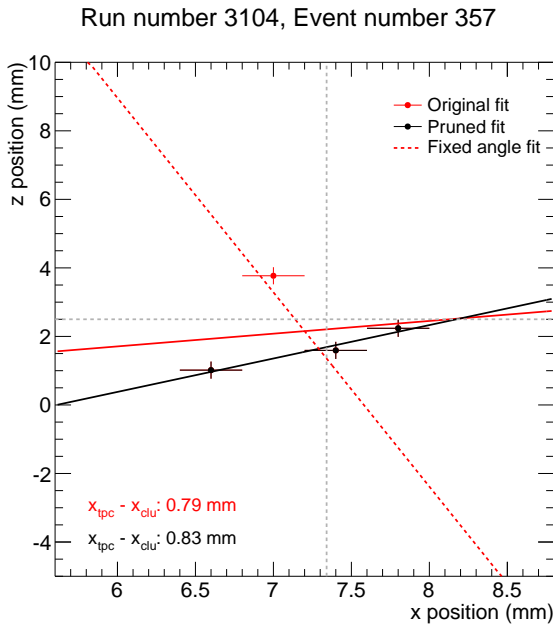


Figure 59: Event display for event 357 of run 3104. In this example, the angle that is fit is very different from the true angle, and pruning does not improve the fit.

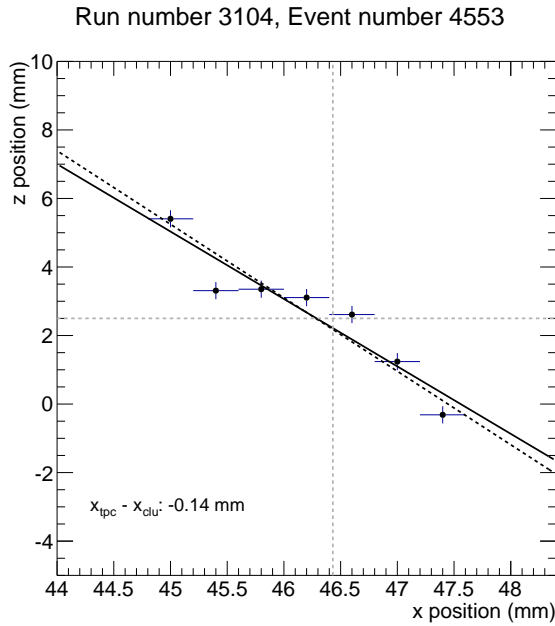


Figure 60: Event display for event 4553 of run 3104. In this example, there are 7 hits and no pruning is necessary. The fitted μ TPC center is 0.14 mm from the barycenter.

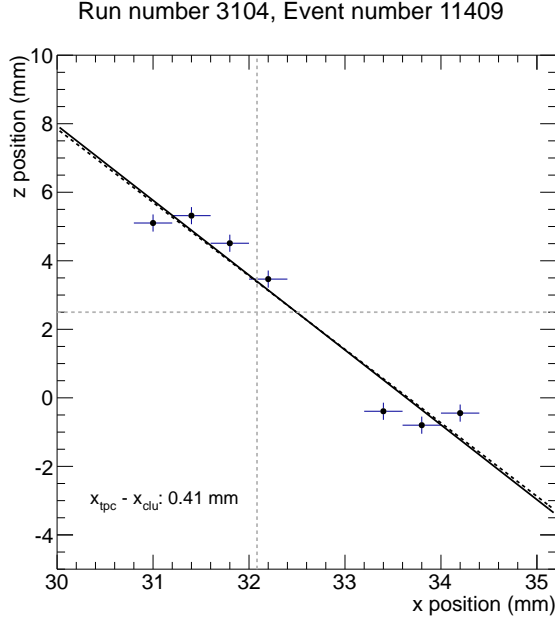


Figure 61: Event display for event 11409 of run 3104. In this example, there are 7 hits and no pruning is necessary. There are also some holes in the center of the cluster. The fitted μ TPC center is 0.41 mm from the barycenter.